ΠΑΝΕΠΙΣΤΗΜΙΟ ΚΡΗΤΗΣ
UNIVERSITY OF CRETE

ΠΟΛΥΤΕΧΝΕΙΟ ΚΡΗΤΗΣ
TECHNICAL UNIVERSITY OF CRETE

FORTH
FOUNDATION FOR RESEARCH AND TECHNOLOGY - HELLAS

# ΤΡΙΔΙΑΣΤΑΤΗ ΕΚΤΥΠΩΣΗ ΠΟΛΥΜΕΡΙΚΩΝ ΜΙΚΡΟΡΕΥΣΤΟΝΙΚΩΝ ΣΥΣΚΕΥΩΝ

**ΜΕΤΑΠΤΥΧΙΑΚΗ ΕΡΓΑΣΙΑ**

ΥΠΟΒΛΗΘΗΚΕ ΣΕ ΕΚΠΛΗΡΩΣΗ
ΤΩΝ ΑΠΑΙΤΗΣΕΩΝ ΓΙΑ ΤΟ
ΜΕΤΑΠΤΥΧΙΑΚΟ ΔΙΠΛΩΜΑ
ΣΤΗ
**ΒΙΟΪΑΤΡΙΚΗ ΜΗΧΑΝΙΚΗ**


## ΙΑΚΩΒΟΣ ΓΑΒΑΛΑΣ

ΤΜΗΜΑ ΙΑΤΡΙΚΗΣ ΣΧΟΛΗΣ
**ΠΑΝΕΠΙΣΤΗΜΙΟ ΚΡΗΤΗΣ**


ΚΡΗΤΗ, ΙΟΥΛΙΟΣ 2023

Επιβλέπων: Δρ. Εμμανουήλ Στρατάκης

BIOMEDICAL ENGINEERING MSc PROGRAM
UNIVERSITY OF CRETE
TECHNICAL UNIVERSITY OF CRETE
FOUNDATION FOR RESEARCH AND TECHNOLOGY-HELLAS

ΠΑΝΕΠΙΣΤΗΜΙΟ ΚΡΗΤΗΣ
UNIVERSITY OF CRETE

ΠΟΛΥΤΕΧΝΕΙΟ ΚΡΗΤΗΣ
TECHNICAL UNIVERSITY OF CRETE

FORTH
FOUNDATION FOR RESEARCH AND TECHNOLOGY - HELLAS

# 3D PRINTING OF POLYMERIC MICROFLUIDIC DEVICES

**APPLICATION GRADE THESIS**

SUBMITTED IN FULFILMENT
OF THE REQUIREMENTS FOR THE DEGREE OF
MASTER OF SCIENCE
IN
**BIOMEDICAL ENGINEERING**


## IAKOVOS GAVALAS

Department of Medical School
**University of Crete**


Crete, July 2023

Supervisor: Dr. Emmanuel Stratakiσ

BIOMEDICAL ENGINEERING MSc PROGRAM
UNIVERSITY OF CRETE
TECHNICAL UNIVERSITY OF CRETE
FOUNDATION FOR RESEARCH AND TECHNOLOGY-HELLAS

# ΠΡΟΛΟΓΟΣ

Εγώ, ο Γαβαλάς Ιάκωβος, επιβεβαιώνω ότι η εργασία που παρουσιάζεται σε αυτή τη διατριβή είναι δική μου. Οι πληροφορίες που προέρχονται από άλλες πηγές σημειώνονται με παραπομπή.

Η παρούσα διατριβή πραγματοποιήθηκε στο πλαίσιο του Μεταπτυχιακού Προγράμματος στη Βιοϊατρική Μηχανική, υπό την επίβλεψη του Δρ Εμμανουήλ Στρατάκη. Αυτή η διατριβή αποτελεί προϊόν προσωπικής εργασίας και δεν περιέχει τίποτα που να είναι αποτέλεσμα εργασίας τρίτου προσώπου.

# ΕΥΧΑΡΙΣΤΙΕΣ

Αρχικά, θα ήθελα να εκφράσω τις ευχαριστίες μου στον Δρ Ηλία Κούμουλο που με βοήθησε από την πρώτη στιγμή αυτού του Μεταπτυχιακού Προγράμματος. Επιπλέον, είμαι εξαιρετικά ευγνώμων στον Δρ. Εμανουήλ Στρατάκη, ο οποίος πίστεψε σε εμένα από την πρώτη στιγμή. Μετά το τέλος των βασικών σπουδών, έγινα μέλος της ερευνητικής του ομάδας για ένα χρόνο έως ότου έγινα δεκτός στο πρώτο μου Μεταπτυχιακό Πρόγραμμα στο Πανεπιστήμιο Ιωαννίνων. Επίσης, θα ήθελα να ευχαριστήσω την Δρ Μαρία Κιτσαρά, με την οποία είχα την ευκαιρία να συνεργαστώ, όσο ήταν μέλος της BIOG3D. Η Δρ Μαρία Κιτσαρά, με βοήθησε να διευρύνω τις γνώσεις μου στον τομέα της Μηχανικής Ιστών και της Μικρορευστονικής μέσα από τις πολλές επιστημονικές συζητήσεις μας. Επιπλέον, θα ήθελα να εκφράσω τις ειλικρινείς ευχαριστίες μου σε όλους τους συναδέλφους μου στη BIOG3D για την υποστήριξη και την κατανόησή τους κατά τη διάρκεια αυτής της απαιτητικής περιόδου.

Τέλος, θα ήθελα να ευχαριστήσω την οικογένειά μου που στάθηκε δίπλα μου, στήριξε τα όνειρά μου και μου έδωσε τη δύναμη να κυνηγήσω το πάθος μου για την επιστήμη.

# PREFACE

I, Gavalas Iakovos, confirm that the work presented in this thesis is my own. Where information has been derived from other sources, I confirm that this has been indicated in the thesis.

All the work described in this thesis was carried out under the Master program in Biomedical Engineering, under the supervision of Dr. Emmanuel Stratakis. This dissertation is my own work and contains nothing which is the outcome of work done in collaboration with others except as specified in the text and summarised in the Statement of Contributions.

# ACKNOWLEDGEMENTS

First of all, I would like to express my appreciation to Dr. Elias Koumoulos who assisted me from the first time of this Master Programme. In addition, I am extremely grateful for being supervised by Dr. Emanuel Stratakis, who believed in me right after my Bachelor Thesis, when I became part of his research group for one year until I got accepted in my first Master Program at University of Ioannina. Also, I would like to acknowledge Dr. Maria Kitsara, with whom I had the opportunity to collaborate, while she was part of BIOG3D. Dr. Maria Kitsara, helped me to expand my knowledge in the field of Tissue Engineering and Microfluidics through our many scientific conversations. Furthermore, I would like to express my sincere gratitude to all my colleagues in BIOG3D for being so supportive during this demanding period.

Last but not least, I would like to thank my family who stood by me, supported my dreams, and gave me the strength to pursue my passion for science.

*Science does not know*

*its debt to imagination*

*-Ralph Waldo Emerson (1803-1882)-*

# ΠΕΡΙΓΡΑΦΉ

Η τρέχουσα μεταπτυχιακή διατριβή με τίτλο «Τριδιάστατη εκτύπωση πολυμερικών μικρορευστονικών συσκευών» πραγματοποιήθηκε για τους σκοπούς του διεπιστημονικού μεταπτυχιακού προγράμματος Βιοϊατρικής Μηχανικής, που διοργανώθηκε από το Πανεπιστήμιο Κρήτης, το Πολυτεχνείο Κρήτης και το Ίδρυμα Τεχνολογίας και Έρευνας (Ηράκλειο, Κρήτη)

Στο πλαίσιο της παρούσας εργασίας, σχεδιάστηκαν και κατασκευάστηκαν διαφορετικές μικρορευστονικές συσκευές με τη μέθοδο της Προσθετικής Κατασκευής (3D Printing). Πιο συγκεκριμένα, η τεχνική του Φωτοπολυμερισμού Ρητίνης χρησιμοποιήθηκε για την κατασκευή των μικρορευστονικών συσκευών. Επιπλέον, σχεδιάστηκε και κατασκευάστηκε μια εξατομικευμένη αντλία, υποδοχής τριών συρίγγων, για την αξιολόγηση της ροής των υγρών στο εσωτερικών των μικροκαναλιών. Οι μικρορευστονικές διατάξεις που σχεδιάστηκαν και εκτυπώθηκαν με την μέθοδο του 3D printing, επικεντρώνονται στη διφασική παραγωγή σταγονιδίων, γνωστών ως σταγονίδια Janus και στη διαδοχική παραγωγή σταγονιδίων χρησιμοποιώντας μια διπλή διασταύρωση σχήματος-Τ.

Ο σκοπός αυτής της εργασίας είναι να δημιουργηθεί μια απλή και κατανοητή ροή εργασιών που απαιτούνται για τον σχεδιασμό και την κατασκευή μικρορευστονικών διατάξεων χαμηλού κόστους για πιθανές βιοϊατρικές εφαρμογές χρησιμοποιώντας την μέθοδο του 3D printing και μια αντλία υποδοχής τριών συρίγγων, κατασκευασμένη με εξαρτήματα που βρίσκονται σε έναν προσιτό τρισδιάστατο εκτυπωτή.

# ABSTRACT

The current master's Dissertation, entitled "3D printing of polymeric microfluidics devices" was conducted for the purposes of the interdisciplinary master programme of Biomedical Engineering, organized by the University of Crete, the Technical University of Crete and the Foundation for Research and Technology Hellas.

Here, in this study, different microfluidics devices have been designed and tested exploiting additive manufacturing (AM) technology. More specifically, Vat Photopolymerization (VPP) technique was used for the fabrication of the microfluidics devices. Furthermore, a custom-made triple syringe pump was designed and fabricated in order to assess the fluid flow inside the microchannels. The produced microfluidic device is focused on biphasic droplet generation, known as Janus droplets and on consecutive droplet generation utilizing a Double T- junction.

The purpose of this work is to establish a workflow and investigate the feasibility of low cost, 3D printing microfluidic devices for biomedical applications using a custom-made triple syringe pump, made with components found in an affordable 3D printer.

# CONTENTS

## Illustrations

# Tables

## Abbreviations

**AM**: Additive Manufacturing.
**3D**: Three Dimensional.
**3DP**: Three-dimensional printing.
**UV**: Ultraviolet.
**SLA**: Stereolithography Apparatus.
**CAD:** Computer Aided Design.
**STL**: Standard Triangulate or Tessellation Language.
**CAM:** Computer Aided Manufacturing.
**VPP**: Vat Photopolymerization.
**FDF**: Fused Filament Fabrication.
**SLM**: Selective Laser Melting.
**FFF**: Fused Filament Fabrication.
**RepRap**: Replicating Rapid prototyping.
**SLS:** Selective Laser Sintering.
**DMLS**: Direct Metal Laser Sintering.
**EBM**: Electron Beam Melting.
**LCD**: Liquid Crystal Display.
**DLP**: Digital Light Processing.
**µFD**: microfluidic device.
**3DPµFD**: 3D printed microfluidic device.
**PDF**: Pressure Driven Flow.
**PLA**: Polylactic Acid.
**CR**: Clear Resin.
**PP**: polypropylene.
**PB**: Prussian blue nanoparticles.
**PET**: poly(ethylene terephthalate).
**HUVECs**: Human umbilical vein endothelial cells.
**PCLSs**: precision cut liver slices.
**PVA**: polyvinyl alcohol.
**PEG-DA**: Poly (ethylene glycol) diacrylate.
**PDMS**: Polydimethylsiloxane.
**FPAs**: finger-powered actuators.
**BBB**: blood-brain barrier.
**BMECs**: Brain Microvascular Endothelial Cells.
**hiPSCs**: human induced Pluripotent Stem Cells.
**TEER**: trans-endothelial electrical resistance.
**PCL**: polycaprolactone.
**HepG2**: Human hepatocellular carcinoma cells.
**hPSC**: human pluripotent stem cell.

# 1 INTRODUCTION

## 1.1 3D PRINTING

3DP is an additive manufacturing process in which the final functional product is fabricated in a layer-by-layer manner. In 1974, in a regular column in the journal New Scientist [1], Dr. David E. H. Jones, using his pen name Daedalus, which was the fictional inventor of DREADCO Company, was the first who introduced the concept of the 3DP. Due to his scientific and academic background he pointed out that many liquid monomers can be solidified under UV or visible light exposure. Using his imaginary character, Daedalus, he mused a new method for plastic fabrication process, using a laser beam and a set of many mirrors. Six years later, in 1981, after the Dr. David E. H. Jones published his imaginary concept of a new plastic fabrication process, Dr. Hideo Kodama from Nagoya Municipal Industrial Research Institute, published his work in which an automatic method for fabricating a three-dimensional plastic model with photo-hardening polymer, was created [2]. It was the first time a CAD "moved" from a 2D display to a man's hand (Figure 1).

**Figure 1** Chemist Dr. David E. H. Jones, the "prophet" of the 3D printing. Photograph: Conor Lawless.

In 1984, Chuck Hull (Figure 2), the co-founder, executive vice president and chief technology officer of 3D Systems, managed to patent his invention of SLA process using UV lasers to solidify in a layer-by-layer manner, photopolymer solutions. He defined his patent as a "system for generating three-dimensional objects by creating a cross-sectional pattern of the object to be formed on a selected surface" [3].


**Figure 2** (Right) Chuck Hull with a 3D replica miniature of himself and (Left) Chuck Hull with the first commercial SLA 3D printer, SLA-1, made from 3D Systems.

He is also responsible for the STL file format, which was created by 3DSystems, and it is a standard file format in all CAD and CAM software. In 1986, the first commercial VPP 3D printer released with the name SLA-1 [4]. The first FDM 3D printer (Fig. 4), was introduced in 1988 by S. Scott Crump and his wife, Lisa and commercialized by his company Stratasys. The story of their invention is quite unusual because it is not scientific or technological oriented. Scott and Lisa wanted to make a frog toy for their daughter, they used a glue gun loaded with silicon and a candle wax. The toy was created by hand mimicking the stereolithography process by depositing hot silicon layer-by-layer. Few years later he automated the process and patented it under the name of “Fused Deposition Modeling” [5]. The FDM patent expired in 2009 [6]. In 1995, the first SLM 3D printer was fabricated at the Fraunhofer Institute ILT in Aachen, Germany. During the SLM printing, a metallic powder, melts, and fuses on the interaction with a power-density laser. Using the layer-by-layer process, complex metallic geometries are possible to be fabricated that could not be made otherwise [7]. At the dawn of 2000s, 3DP changed dramatically. In 2004 a mechanical engineering lecturer Adrian Bower, started the RepRap project. This was an open-source project in which everyone could download the software, gather the parts, and build the first home-made FFF printer out of inexpensive thermoplastic filaments. The first RepRap printers weren’t so reliable, but as the years go by and the 3D printing gained more and more enthusiasts, printers based on RepRap project, are coming out wonderful. In 2009, the first low-budget commercial 3D printer, based on the RepRap project, was sold to the public the “Makerbot” (Figure 3) [5].

Additive manufacturing, starting in the 1980s, has expanded rapidly. Different materials, a variety of 3D printing techniques and the “open source” culture, led the field to evolve in many directions. Three basic 3D printing techniques dominate the global market: VPP, FFF and Powder-Bed Methods such as SLM, SLS, DMLS, EBM and many more. Despite the different techniques, the invariable factor, is the computer control of the process. Thus, 3D printing is considered part of robotics. Here, for the purpose of this study, of 3DP μFDs, only VPP and FFF 3DP processes will be discussed.

**Figure 3** MakerBot founders (left to right) Adam Mayer, Zach Smith and Bre Pettis with the final MakerBot Cupcake prototypes.

## 1.1.1 STEREOLITHOGRAPHY APPARATUS (VPP)

As mentioned above, VPP was first introduced by Chuck Hull and his company, 3D Systems, in 1986. It was the first commercialized additive manufacturing technique. And it is still one of the most common layer-by-layer 3D printing methods. VPP as a more general term includes SLA, LCD and DLP 3DP systems (Figure 4 (I). In, this study, a LCD 3D printer is employed. During the printing process with a LCD machine, an UV LED array lights up and emits radiation towards the bottom of a transparent tank (resin vat). The light emitted from the LED array is guided through a Fresnel Lense which enhance the printing resolution while also improves the efficiency of the light source. A detachable build plate platform can move alongside the z-axis (up and down) and slightly touches the bottom of the transparent tank. When the build platform is few μm above the transparent vat (from 10 to 300 μm), the LCD screen is activated and generates a 2D image of each layer obtained from the slicing software. The pixels corresponding to the solid areas of the object’s cross section, are transparent or semi-transparent (unmasked or partially masked), allowing all or part of the UV light to pass through, towards the total or partial photopolymerization of the photosensitive resin. The amount of the UV light passes through the LCD screen, allows the printing of smoother curved edges (In most of the resin slicer software, this is called as Anti-aliasing). The empty areas of the object’s cross section

are blocked (black, masked pixels) prohibiting the UV light penetration towards the resin vat. (Figure 4 (II)) The photopolymerization/solidification of each cross section occurs in the interface between the transparent vat and the build platform. Then, the elevated platform moves slightly upwards and another layer of photocured resin is added to the previous one. The whole process continues through the end and the designed 3D model is finally appeared strongly attached on the surface of the build platform [8]. Using any VPP machine, supporting structures are required to overcome the gravitational forces acting on the printed model. While VPP technique can produce objects with extreme details, with resolution often smaller than 100μm, it also requires extensive post processing. Once the model is completed, an organic solvent such as isopropyl alcohol is used to remove any excess, non-photopolymerized resin material from the surface of the 3D printed object. Then, photocuring process is taking place and the remaining resin solidifies. The 3D printed component becomes mechanically and chemically stable. Supports are then removed manually and the remaining support marks are cleaned. Several advantages and disadvantages of the VPP process are depicted in the table below (Table 1) [9].

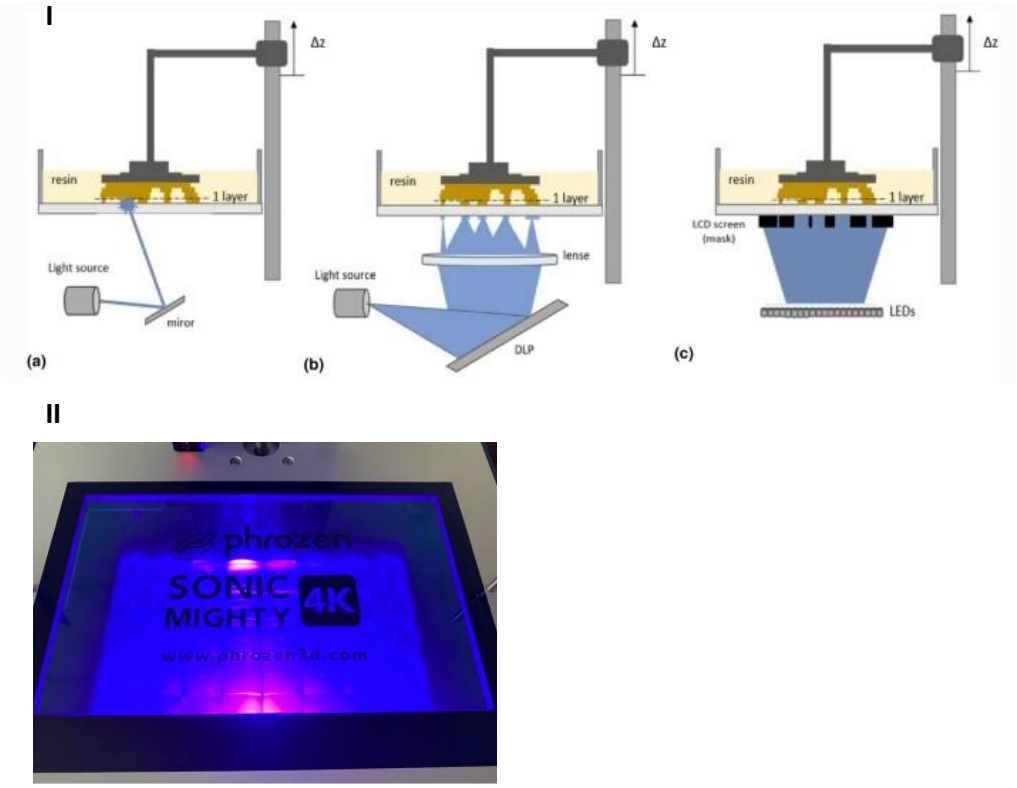


**Figure 4** (I) A graphical representation of the 3 most used VPP 3D printing technologies (a). SLA (b). DLP and (c). LCD 3D VPP resin 3D printer [8] (II) a photograph from the LCD screen of the Phrozen Sonic Mighty 4K, in which the printing areas are transparent while the blocked areas are masked with black pixels (Source: www.phrozen3d.com ).

**Table 1** Advantages and Disadvantages of VPP 3D printing

| a/a | Advantages | Disadvantages |
|---|---|---|
| 1 | Operates unattended | Post curing |
| 2 | Wide range of build volumes | Post processing |
| 3 | Printing Accuracy | Weaker than the injection molding parts |
| 4 | High quality surface finish | Degrade in sunlight |
| 5 | A lot of available materials | Difficult to use multiple materials in a single print |
| 6 | Printing multiple parts simultaneously | Resin and Solvent toxic wastes |
| 7 | Ease to operate | Final parts are sensitive to long UV exposure time |
| 8 | Usually no calibration is required | Expensive Equipment |

## 1.1.2 FUSED FILAMENT FABRICATION (FFF)

Unlike VPP 3DP, which photocures light sensitive resins, FFF process uses thermoplastic filaments which are extruded from a heated nozzle and placed on a build platform layer by layer. A FFF 3D printer is mainly consisted of a filament extrusion system (also known as extruder). There are two popular types of extruders, Bowden, and Direct Drive (Figure 5). Bowden extruder is placed on the printer's frame. It is connected with the hot end through a long (polytetrafluoroethylene) PTFE Bowden tube. Unlike a Bowden extruder, a Direct extruder is mounted directly on to the hot end and the filament travels a small distance from the extruder to the nozzle.

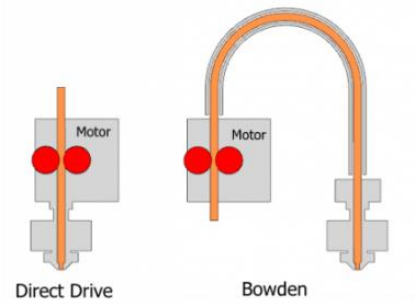


**Figure 5** Direct Vs Bowden extruder. http://www.spiderbot.eu/direct-drive-bowden-remote-motor-the-differences/?lang=en

The hot end and the printing head is the most complex part. It deals with the melting and extruding the thermoplastic filament. For the hot end design, a standard knowledge of the thermal properties and the glass transition temperature of the material is required. The filament exits through a metallic nozzle and is placed upon the build platform. Nozzles from different materials and with variety of diameters, lengths and shapes exist. The build platform is the surface on which the 3D model is printed, can be heated or not to sustain the printing process. Several advantages and disadvantages of the FFF process are depicted in the table below (Table 2) [9]

**Table 2** Advantages and Disadvantages of FFF 3D printing

| a/a | Advantages | Disadvantages |
|---|---|---|
| 1 | Inexpensive equipment | Weak layer Adhesion |
| 2 | Most widespread AM technology | Inefficient for mass production |
| 3 | Ideal for prototyping | Longer printing time |
| 4 | No complex mechanisms | Rough surface finish |
| 5 | Compact design | Particles emission during printing |
| 6 | Materials variation | Machine calibration is needed (bed and extruder) |
| 7 | Reusable filaments | Warping |
| 8 | Usually no extensive post process is required | Nozzle clogging |

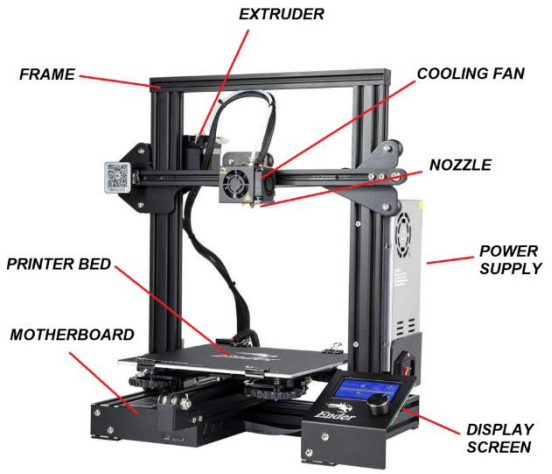


**Figure 6** FFF main components. Printer: Creality Ender 3

# 1.2 MATERIALS

There is a variety of materials used in AM technology covering filaments, resins, powders, clay, cements, hydrogels and even food. However, this study focuses on the materials utilized in VPP and FFF 3DP technology.

### 1.2.1 The chemistry of VPP materials.

The idea behind the VPP process is to use monomers and/or oligomers in a liquid state which can be photopolymerized upon exposure to a certain wavelength and form a thermoset material. For the photopolymerization process to occur, photoinitiator molecules are required to absorb the photons energy and generate free active radicals or cations towards the polymeric chain growth. The conventional materials used in VPP dictate a non "living" polymerization mechanism, meaning that the polymerization is terminated when light exposure is off [10]. In VPP process, the light source employed to provide the necessary photon energy to the photoinitiators can be LEDs, Lasers, xenon lamps even mercury arc lamps. The wavelength of these light sources is within 190nm to 1000nm. Since the majority of the commercially available VPP 3D printing systems operate using a 405nm light source, only the photoinitiators sensitive to the near UV and visible wavelengths will be analysed. The most used photoinitiators in the SLA and DLP market are: TPO (2,4,6-trimethylbenzoyldiphenylphosphine oxide) and phenylbis(2,4,6-trimethylbenzoyl) phosphine oxide (BAPO or Omnicure 819, also known as Irgacure 819) (Figure 7) [11]

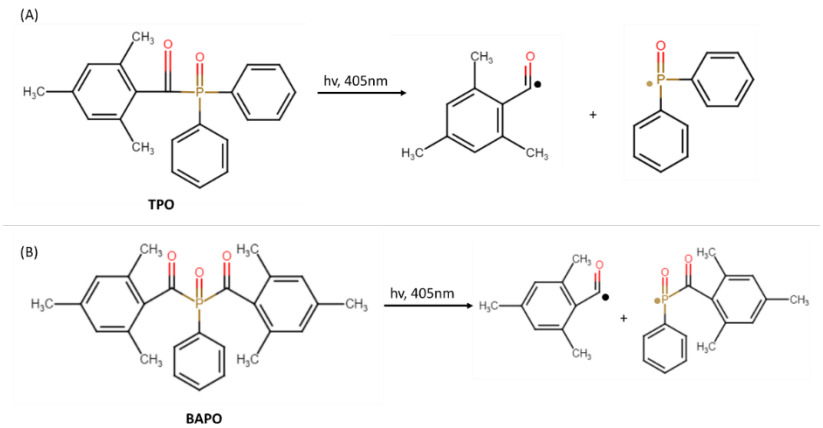


**Figure 7** TPO and BAPO molecules. Free radicals production when incident light is absorbed.

The photopolymerization process in VPP resins can be divided into three stages: initiation, propagation, and termination (Fig. 1.8). Exposure to UV light excites the photoinitiator molecules during the initiation stage. This produces highly reactive free radicals, which can initiate the polymerization reaction by attacking the double bonds in the monomer molecules. The polymerization reaction enters the propagation stage once it has begun. In this stage, the reactive free radicals produced during the initiation stage continue to attack double bonds in monomer molecules, resulting in the formation of polymer chains. Finally, the polymerization reaction reaches the termination stage, where it slows and eventually stops. As more monomer molecules are consumed in the formation of polymer chains, the number of free radicals available to initiate new polymerization reactions decreases. The VPP resin hardens into a solid object as the polymer chains continue to grow and crosslink with one another. The final object's properties will be determined by several factors, including the resin composition, the intensity and duration of the UV light exposure, and the printing parameters used. Monomers and oligomers play a critical role in the process of SLA 3D printing as they are the building blocks that combine to form the final polymerized structure of the 3D printed object. Monomers are small, reactive molecules that can combine with each other to form long chains called polymers while oligomers are larger molecules that have already started to form polymer chains but are not yet fully polymerized [12]. In SLA 3D printing resins, the monomers and oligomers are combined with photoinitiators to create a liquid that hardens when exposed to UV light. The specific combination of monomers and oligomers used in the resin will affect the properties of the final 3D printed object, including its strength, flexibility, and resistance to environmental factors. Some of the most used monomers in commercially available SLA 3D printing resins include, Styrene, Methyl methacrylate (MMA) and Acrylate. Styrene, is a highly reactive monomer that can form polymers with a high degree of cross-linking, making it well-suited for creating rigid and durable 3D printed objects. MMA-based resins can produce objects with good mechanical properties, including strength and toughness (such as Formlabs Clear Resin v4, FCRv4)[1] while Acrylate-based monomers are known for their excellent UV resistance, making them a good choice for 3D printed objects that will be exposed to sunlight. Two of the most used oligomers in SLA 3D printing resins are i) the Epoxy acrylates which are highly cross-linked oligomers, leading to 3D printed objects that are highly resistant to chemical and environmental factors and ii) the Polyurethane acrylates that are highly flexible, making them well-suited for creating 3D printed objects that require a degree of elasticity (such as Crystal Clear Resin, PrimaCreator, CCPC)[2].

[1] https://formlabs-media.formlabs.com/datasheets/Safety_Data_Sheet_EN-EU_-_Clear.pdf
[2] https://cdn.shopify.com/s/files/1/2424/8853/files/Material_safety_data_sheet_RESIN-EN-2022.pdf?v=1668689721

### 1.2.2 The chemistry of FFF materials.

While the VPP method utilizes photocurable resins (thermoset materials), FFF uses thermoplastic materials. Thermoplastic materials possess the unique property of being able to soften and flow when heated to their melting point, and then solidify again when cooled. This process of melting and solidification is fully reversible, meaning that thermoplastics can be heated and cooled multiple times without undergoing any significant chemical changes. These properties make thermoplastics highly versatile and suitable for a wide range of manufacturing processes, including injection moulding and FFF [13]. Specifically, the ability to melt and flow under heat enables thermoplastics to extrude from the heated nozzle of the 3D printer and solidify upon cooling under the air flow from the fan which is located next to the nozzle. Some of the most common commercially available thermoplastic materials for FFF are Acrylonitrile Butadiene Styrene (ABS), polylactic acid (PLA) and Polycarbonate (PC) as they are depicted in Table 3. Composite thermoplastics are also available, expanding the capabilities of 3DP in industry.

**Table 3** List of the most common commercially available FFF materials[3]

| Material | Name | Source | Advantages | Disadvantages | Printing Temperature Range |
|---|---|---|---|---|---|
| ABS | Acrylonitrile butadiene styrene | Petroleum | Good impact resistance, toughness, | prone to warp, produce unpleasant gases | 210-250 |
| PLA | Polylactic Acid | Plant starch | Biodegradable, does not warp, Inexpensive | poor mechanical rough texture, brittle | 190-230 |
| PC | Polycarbonate | Bisphenol | Strong and flexible, good optical properties | High print temperature, absorb moisture | 260-310 |

## 1.3 MICROFLUIDIC DEVICES (μFD)

The fluid inside a microfluidic channel can be considered continuum with a known density at any point. This assumption is an effective tool to explain and mathematically describe several of transport phenomena without deep knowledge of their internal molecular structure. Transport phenomena (momentum transfer, energy transfer and mass transfer) play an essential role in the microfluidics field governing the design and the behaviour of the microfluidic device. In microfluidics, several thermodynamic (like

[3] Dey, A., Roan Eagle, I. N., & Yodo, N. (2021). A Review on Filament Materials for Fused Filament Fabrication. *Journal of Manufacturing and Materials Processing, 5*(3), 69. https://doi.org/10.3390/jmmp5030069

pressure, density, and temperature) and mechanical (like viscosity, shear stress and surface tension) fluid properties need to be considered in order to design and fabricate a well-functioning device. Furthermore, dimensionless numbers (Table 4) [14] are of great importance in microfluidics. They can simplify complex fluids problems and they can compare the importance of forces, energies and time scales that take place.

**Table 4** List of relevant dimensionless numbers in microfluidics [14]

| **Dimensionless Number** | **Equation** | **Description** | **Symbols** | **Characteristics** | **Applicability** |
|---|---|---|---|---|---|
| Reynolds Number (Re) | $R_e = \frac{\rho U L}{\mu}$ | Ratio of inertial to viscous forces | ρ: fluid density<br>U: characteristic velocity<br>L: characteristic length scale<br>μ: dynamic viscosity | Determines flow regime (laminar or turbulent) | Flow of fluids in microchannels |
| Peclet Number (Pe) | $P_e = \frac{UL}{D}$ | Ratio of advection to diffusion timescales | U: characteristic velocity<br>L: characteristic length scale<br>D: diffusion coefficient | Determines importance of advection vs. diffusion | Transport and mixing of molecules in microfluidic systems |
| Schmidt Number (Sc) | $S_c = \frac{\mu}{\rho D}$ | Ratio of momentum diffusivity to mass diffusivity | μ: dynamic viscosity<br>ρ: fluid density<br>D: diffusion coefficient | Describes mass transfer of a scalar quantity in a fluid | Mass transport in microfluidic devices |
| Weber Number (We) | $W_e = \frac{\rho U^2 L}{\sigma}$ | Ratio of inertial to surface tension forces | ρ: fluid density<br>U: characteristic velocity<br>L: characteristic length scale<br>σ: surface tension | Determines breakup of droplets or bubbles | Droplet and bubble formation in microfluidics |
| Capillary Number (Ca) | $C_a = \frac{\mu U}{\sigma}$ | Ratio of viscous to surface tension forces | μ: dynamic viscosity<br>U: characteristic velocity<br>σ: surface tension | Describes deformation and breakup of droplets or bubbles | Paper microfluidics, Droplet, and bubble formation in microfluidics |

***Navier-Stokes Equation***

The fluid flow inside a microfluidic channel can be described using the Navier-Stokes equation (N-S) eq. (1.1):

$$\rho\left[\frac{\partial\vec{u}}{\partial t}+\vec{u}\nabla\vec{u}\right]=-\nabla P+\mu\nabla^2\vec{u}+\overrightarrow{f_{ext}}\,, \tag{1.1}$$

where ρ is the fluid's density, u is the velocity field, P is the pressure, μ, is the dynamic viscosity of the fluid and $\overrightarrow{f_{ext}}$ is the external forces acting on the fluid flow. The N-S eq. is a second-order nonlinear Partial Differential Equation (PDE) and there is no analytical solution. However, assumptions required to transform the complex N-S eq. into a simpler form to obtain an analytical solution. The complexity of the equation comes from the $\rho\vec{u}\nabla\vec{u}$ term that makes the N-S eq. nonlinear. However, computational Fluid Dynamics (CFD) methods can be utilized to solve numerically the N-S eq.

***Microfluidics Resistance***

When a fluid flows inside a microfluidic channel it experiences resistance to its flow due to the channel's characteristics. This happens due to the dominant viscous effects compared to inertia. In analogy to electrical circuits (Table 4), the pressure, P, can be considered to be the potential, ΔV. The flow rate, Q, could be related to the electric current, I while the flow resistance, R, can be considered to be the electrical resistance.

**Table 5** Comparison between Microfluidics and Electrical Circuits

| Microfluidics | Units | Electricity | Units |
|---|---|---|---|
| Pressure | Pa | Potential | V |
| Flow Rate | $m^3/s$ | Electric Current | A |
| Resistance | $Pa\cdot s\cdot m^{-3}$ | Resistance | Ω |

***Microfluidics Assumptions***

In microfluidics, the fluid flow velocities are often much smaller than the velocity at which sound (or pressure) waves propagate in fluids, under this assumption the fluid can be treated as **incompressible**. The incompressibility of the fluid flow does not imply that the fluid itself is incompressible. In an incompressible flow, the density of the fluid remains constant within a parcel of a fluid when it moves with the fluid flow velocity. This means that the density does not change in space and time. Eq. (1.2) represents the Continuity Equation in fluid dynamics. Furthermore, for Newtonian and incompressible fluids, unidirectional flow and steady state phenomena are often dominant and the $\overrightarrow{f_{ext}}$ due to gravity can be neglected since $\rho\vec{g} \ll \overrightarrow{f_{pressure}}+\overrightarrow{f_{viscous}}$.

$$\frac{\partial\rho}{\partial t}+\nabla\rho\vec{u}=0\,. \tag{1.2}$$

The time derivative is related to the loss of mass in the system while the divergence describes the difference between the inlet and the outlet of the fluid flow. For an incompressible fluid, the $\frac{\partial \rho}{\partial t}$ term can be neglected, and the Continuity Equation can be written as:

$$\nabla \vec{u} = 0 \,, \tag{1.3}$$

that means that the velocity field divergence is zero at any point. When the fluid flow is considered to be **steady state** (time independent) the velocity gradient becomes zero,

$$\frac{\partial \vec{u}}{\partial t} = 0 \,, \tag{1.4}$$

and the Eq. (1.5) can be simplified as:

$$\nabla P = \mu \nabla^2 \vec{u} \,. \tag{1.5}$$

The above Eq. (1.8) is also known as the **Stokes Equation** and can be used instead of N-S eq. when the aforementioned assumptions met.

***Fluid Flows***

As mentioned above, the N-S eq. is the governing equation for the fluid flow. However, no analytical solutions exist since the nonlinearity of the PDE. Although, using specific assumptions, useful fluid flow cases can be described. Pressure Driven Flow (PDF) (Fig 1.3) is the most used case in microfluidic devices and the one we are going to use in the 3D printed microfluidic devices.

***Pressure Driven Flow***

In the Pressure Driven Flow, the fluid flows inside the microfluidic channel due to the pressure drop (pressure difference) between the inlet and the outlet. This case of fluid flow is known as **Poiseuille Flow** (or Hagen – Poiseuille flow) (Figure 8). Applying specific Boundary Conditions (B.C) in the pressure driven flow, an analytical solution can be found.

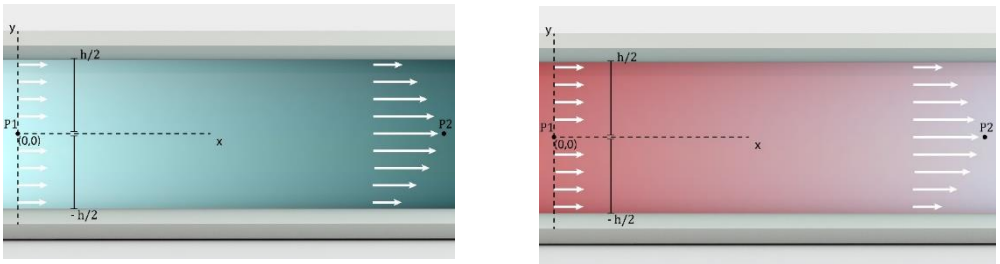


**Figure 8** Fluid flow between two parallel infinite plates. (Left) The blue gradient represents the velocity increase from left to right, while (Right) the red gradient indicates the pressure drop form a higher-pressure point $P_1$ to a lower pressure point $P_2$.

The velocity, close to the microfluidics' walls can be considered to be 0. This B.C is known as no-slip condition, where $\vec{u}\left(y = \pm\frac{h}{2}\right) = 0$. Furthermore, assuming that the flow is Steady-State, $\frac{\partial}{\partial t} = 0$, incompressible, $\nabla\vec{u} = 0$, unidirectional, fully Developed, and axisymmetric, the N-S eq. (1.1) can be solved, and the velocity distribution profile can be described as:

$$0 = -\nabla P + \mu\nabla^2\vec{u}\,, \tag{1.6}$$

$$\nabla^2\vec{u} = \frac{\nabla P}{\mu}\,, \tag{1.7}$$

$$\frac{\partial^2 u}{\partial x^2} + \frac{\partial^2 u}{\partial y^2} + \frac{\partial^2 u}{\partial z^2} = \frac{\partial P}{\mu\partial x}\,, \tag{1.8}$$

Since the problem is 2D and there is no *z-direction*, then the term $\frac{\partial^2 u}{\partial z^2}$ can be neglected. Also, since in the *x-direction* the velocity remains constant, then eq. (1.8) yields:

$$\frac{\partial^2 u}{\partial y^2} = \frac{\partial P}{\mu\partial x}\,, \tag{1.9}$$

eq. (1.9) dictates that the velocity depends only on *y*, but the pressure is only depended on *x*. That means that the Pressure derivative is constant and can be written as:

$$\frac{\partial P}{\partial x} = -\frac{\Delta P}{\mu L}\,. \tag{1.10}$$

If we apply the eq. (1.10) into the eq. (1.9), then.

$$\frac{\partial^2 u}{\partial y^2} = -\frac{\Delta P}{\mu L}\,. \tag{1.11}$$

Solving the above second order PDE one can find that:

$$u(y) = -\frac{\Delta P}{2\mu L}y^2 + c_1 y + c_2\,. \tag{1.12}$$

In order to solve the above equation, we have to recall the B.C of the problem. The velocity close on the walls is zero, thus $\vec{u}\left(\pm\frac{h}{2}\right) = 0$ and two equations are formed.

$$0 = -\frac{\Delta P}{2\mu L}\left(\frac{h}{2}\right)^2 + c_1\frac{h}{2} + c_2\,, \tag{1.13}$$

$$0 = -\frac{\Delta P}{2\mu L}\left(-\frac{h}{2}\right)^2 - c_1\frac{h}{2} + c_2\,, \tag{1.14}$$

By adding these two equations, the $c_2$ is:

$$c_2 = \frac{\Delta P}{8\mu L} h^2 \,. \tag{1.15}$$

Plugging the eq. (1.15) into eq. (1.13), the $c_1$ is

$$c_1 = 0 \,. \tag{1.16}$$

Thus the eq. (1.12) becomes:

$$u(y) = -\frac{\Delta P}{2\mu L} y^2 + \frac{\Delta P}{8\mu L} h^2 \,. \tag{1.17}$$

And the velocity profile can be described by:

$$u(y) = \frac{\Delta P}{2\mu L}\left[\left(\frac{h}{2}\right)^2 - y^2\right]. \tag{1.18}$$

Eq. (1.18) shows that the velocity distribution inside a microfluidic channel, has a parabolic profile. The velocity reaches its maximum value at the centre of the channel when $y = 0$. Then from the eq. (1.18), the maximum velocity is:

$$u_{max}(y) = \frac{\Delta P}{2\mu L}\left(\frac{h}{2}\right)^2 . \tag{1.19}$$

The mean velocity ($\bar{u}(y)$) of the fluid due to the axisymmetric nature of the problem, can be found as:

$$\bar{u}(y) = \frac{u_{max}(y)}{2} . \tag{1.20}$$

The fluid enters the channel with an initial velocity $u_1$. This velocity is equal to the mean velocity in a fully developed flow, thus $u_1 = \bar{u}$. So, the velocity at the exit point is two times the initial fluid velocity, eq. (1.21)

$$u_{out} = 2u_{in} \,. \tag{1.21}$$

The volume flow rate can be found as:

$$Q = \bar{u}A \,, \tag{1.22}$$

where, $A$, is the microchannel's cross-section. From the above, the pressure drop yields:

$$\Delta P = \frac{128\mu L Q}{\pi h^4} . \tag{1.23}$$

# 2 STATE OF THE ART

Microfluidics has revolutionized the field of fluid manipulation and analysis, enabling precise control over small volumes of fluids. Traditional fabrication techniques for microfluidic devices, such as lithography, have limitations in terms of cost, time, and design flexibility. However, the emergence of 3D printing has opened new avenues for rapid prototyping and customization of microfluidic devices.

Among the different processes available, FFF technique is a simple, inexpensive, and more accessible to most laboratories. Thermally extruded polypropylene (PP) has been demonstrated by researchers to be capable of producing tiny reaction ware for organic, inorganic, or materials synthesis, with cheap material cost and rapid construction [15]. Another study revealed the use of a desktop FFF printer to create a Y-shaped mixing microfluidic chip, allowing the synthesis of Prussian blue nanoparticles (PB). A poly (ethylene terephthalate) (PET) filament was used to make the channels transparent, and the device included a PB-modified electrode for H2O2 sensing (Figure 9) [16]. Similarly, utilizing FFF, a basic microfluidic device using translucent PLA was constructed, allowing conventional liquid pumping through threaded ports (Figure 10) [17]. This device was used to make monodisperse microspheres for encapsulating stem cells in alginate droplets. Furthermore, researchers have investigated the use of multiple orientations to control fluidic behaviour on a millimetre scale, in addition to transparency, which is critical for many biological applications. They have used surface roughness, which is commonly seen as a restriction of FFF, to increase fluid mixing (Figure 11) [18]. Human umbilical vein endothelial cells (HUVECs) and precision cut liver slices (PCLSs) were exposed to 12 FFF 3D printing materials to test their compatibility. Despite of its wide use in different medical studies [19], only polyvinyl alcohol (PVA) was found to have considerable cytotoxicity. Possible due to its high solubility in the aqueous medium. While other polymers such as PLA, ABS, and PET had no negative impact on cell survival [20]. A FFF 3D printed microfluidic device exploited capillary forces, was fabricated, and used to create a programmable microfluidic device for co-culture of macrophages and osteoblasts [21].

Although FFF is a cost-effective method of producing microfluidic devices, it may not be appropriate for some biological applications that require small inner fluidic channels, smooth surfaces, and great transparency for to promote real time observations. To circumvent these restrictions, various 3D printing technologies like VPP have been explored [22]. Modular and reconfigurable components with micrometre-sized channels have been designed to emulate electrical circuit architecture, providing diverse microfluidic operations such as adjustable mixing and droplet formation [23]. Utilizing commercially accessible 3D printers, transparent monolithic microfluidic devices with better minimal cross-sectional areas have also been created [24]. Researchers have created custom VPP resins towards the improvement of printing resolution. Poly (ethylene glycol) diacrylate (PEG-DA) and PDMS-methacrylate macromers, for example, allow for the printing of highly transparent and elastomeric microfluidics [25,26]. VPP is limited to printing a single

material limiting geometric and end-use complexity. However, a recent study a brand-new method of 3D printing that uses upconversion photoluminescence to enable multi-material stereolithography. This method allows for the creation of complex 3D structures with multiple materials using a single immersion process. The authors also highlighted the potential applications of this technology in fields such as microfluidics, optics, and biomedicine [27].

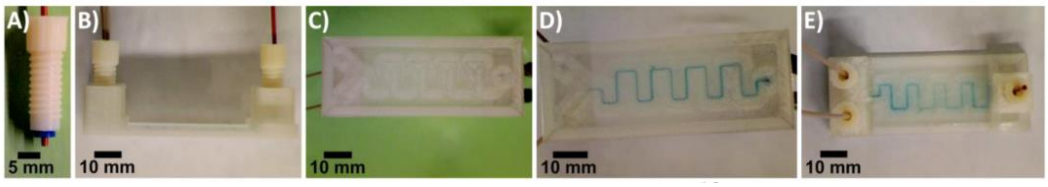


**Figure 9** A 3D-printed Y-shaped mixing device. Images of (A) a 3D-printed ABS fitting, (B) side view of the device, (C and D) bottom views of the device (C) before and (D) after mixing 5 mM iron (II) chloride and 5 mM potassium ferricyanide solutions to form citrate-PBNPs, and (E) top view of citrate-PBNP-filled device [16].

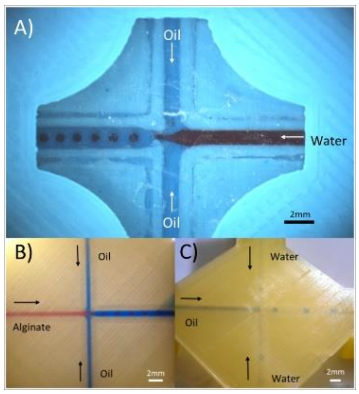


**Figure 10** FFF 3D printed microfluidic device with flow focusing junctions. [17].

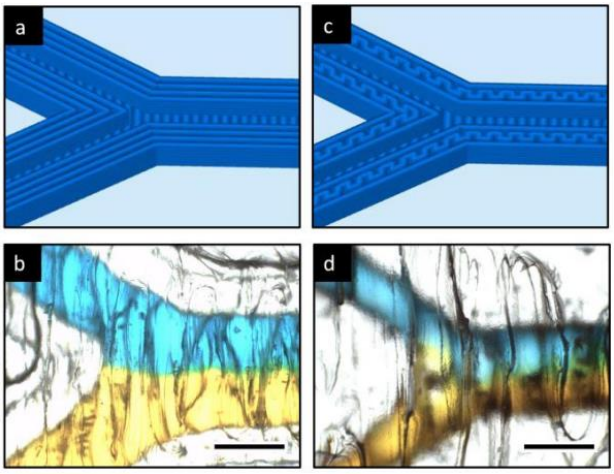


**Figure 11** Comparison of the printing using 4 loops (a, b), and with 2 loops (c, d) in fabrication. a) and c) are schematic showing the movement path of printing nozzle, b) and d) are microscopic images of microchip filled with dyes showing the channel dimension difference, the scale bar is 500 μm [17].

**Biocompatibility of 3D-printed microfluidics:**

Compared to conventional microfabrication methods, 3DPμFD for cell biology studies offers reduced costs and increased accessibility without compromising chip complexity. Therefore, a critical factor is to minimize potential material-induced toxicity when directly printed devices are used for cell culture. It's important to note that the biocompatibility of the device largely depends on the materials used, such as resin and photoinitiators employed in SLA-based 3D printing. Piironen et al. conducted a comprehensive examination of the biocompatibility of four commercially available stereolithography materials from Formlabs [28]. They found that even ISO-certified materials exhibited certain chronic cytotoxicity, particularly impeding the proliferation of 3T3 cells. However, autoclaving the device ensured cell proliferation, suggesting that autoclaving is a critical post-treatment step for supporting long-term cell growth. Similarly, Egger et al. demonstrated that various commercial materials used in SLA printing could induce long-term cytotoxicity over a span of four days [29]. Gelatine methacryloyl (GelMA), a photo-crosslinkable hydrogel containing cells, has also been patterned and evaluated within a 3DPμFD to mimic a 3D biological environment [30]. The results showed acceptable cell viability and proliferation over 5-7 days of dynamic incubation within the 3DP resin-based device. To mitigate potential side effects on cell immobilization, PDMS and PS were used to coat 3D-printed microchannels [31]. Other resin-based materials with biocompatibility have been employed for fabricating microfluidics for cell culture. For example, Tuan et al. demonstrated a 3DPμFD for studying osteoarthritis by recreating the "chondral" and "osseous" microenvironment. Non-cytotoxic Eshell 300 resin was used with SLA to fabricate the 3D bioreactor structures, allowing distinct chondral and osseous zones within the same chamber by controlling media exposure [32]. The same materials were also used for co-culturing mesenchymal stem cells and endothelial cells [33].

**3D printed microfluidics for Lab-on-a-chip applications:**

In the field of microfluidics, the integration of active components like valves and pumps with real-time control and automation is crucial for advancements in cell biology and molecule measurements [34, 35]. However, large-scale integration in microfluidics increases the complexity and consequently the fabrication costs. Soft lithography-based techniques have been traditionally used for fabricating active elements such as valves, but they are expensive due to labour-intensive processes involving moulding, aligning, bonding, and assembling different layers. 3D-printed systems offer a solution to these challenges by minimizing labour processing and eliminating human errors during prototyping. For example, Woolley, Nordin, and colleagues created a microfluidic device with pneumatic valves using 3D printing, utilizing a 50 μm membrane layer. They characterized the device, achieved a 10% volume downscale ratio, and developed integrated micro gasket sets. The 3D-printed pneumatic valves were further reduced in size, with membrane diameters as small as 300 μm to 46 μm and functional squeeze valves as small as 15 mm × 15 mm [36-40]. These advancements in 3D printing have made the size and density of integration in microfluidic devices comparable to traditional multi-layer soft

lithography-based methods. Integrated microfluidic cell culture allows for long-term monitoring under controlled microenvironments. For instance, Folch and colleagues utilizing SLA, managed to incorporate diaphragm valves, peristaltic pumps, and on-chip cell-culture chambers [41]. The pneumatically activatable valve they developed consisted of a 100 μm thick membrane with a diameter of 10 mm, which could be separately controlled by pressurization. They successfully controlled the stimulation of live CHOeK1 cells for analysing calcium ion transportation within the cell using a printed chip with a four-valve switch. Wu and colleagues, have introduced manually actuated components tailored for 3D-printed chips, including torque-actuated pumps and valves [42]. A recent development by McAlpine and his team introduced a 3D printing methodology for fabricating self-supporting microfluidic structures using viscoelastic inks [43]. By carefully designing the filament stacking orientations and utilizing acetoxy silicone as the printing ink, they successfully printed various functional microfluidic devices, including mixers, salinity sensors with herringbone ridges, and sensing electrodes. They even demonstrated an integrated microfluidic valve system on a spherical surface, enabling the realization of microfluidic hybrid sensor chips and the direct 3D printing of physiological and wearable sensors on human skin.

**3D printed microfluidics for Organ-on-a-chip applications:**

The incorporation of three-dimensionality provided by 3D printing has facilitated the recapitulation of organ models, which involve complex geometries and specific microenvironments that enhance cell proliferation and differentiation. The precise recreation of in vitro models using 3D-printed microfluidics has been employed to study organ and organoid development, including aspects like correct morphology, cell-cell/cell-extracellular matrix interactions, and specific gradients, within organ-on-a-chip applications. Organ-on-a-chip technology utilizes our understanding of human organ anatomy to engineer living constructs in vitro, where cells and their microenvironment are precisely arranged to mimic specific aspects of human organs in vivo. A microfluidic blood-brain barrier (BBB) model that mimics in vivo functions, developed by Shuler and colleagues, enabling in vitro drug permeability studies under perfusion [44]. The model involved co-cultivating brain microvascular endothelial cells (BMECs) derived from induced human pluripotent stem cells (hPSCs) with rat astrocytes on a 3D-printed microfluidic device, where all three layers of the device were fabricated using stereolithography with clear resin (Fig. 9a). This configuration allowed integrated electrodes on the device to measure trans-endothelial electrical resistance (TEER) as an evaluation of BBB barrier tightness. To mimic the neuron networks, Lind et al. employed a hybrid additive fabrication approach combining conventional soft lithography and PDMS extrusion printing. This approach allowed the creation of neighbouring compartments with arbitrarily complex designs, eliminating the need for manual post-processing steps like cutting, punching, and bonding that may introduce unwanted artifacts [45]. The authors demonstrated that these compartmentalized devices were suitable for long-term studies of stem cell-derived neurons and astrocytes, with communication channels facilitating neurite entry (Fig. 9b). In another study, Cho et al. developed a bioprinting-based method for one-

step generation of heterotypic cell-laden gels deposited in a printed polycaprolactone (PCL) microfluidic channel [46]. Human hepatocellular carcinoma (HepG2) cells and HUVECs were printed within collagen type 1 and gelatine hydrogels, respectively, in the channel. Continuous medium flow was perfused throughout the printed device to simulate a liver-on-a-chip system. Co-culturing liver and endothelial cells in the channel enhanced metabolic activity and increased albumin and urea production. Alternatively, Jin et al. developed a novel preset cartridge for heterogeneous 3D bioprinting, enabling the emulation of the structure of the human hepatic lobule [47]. Browne et al. developed an indirect 3DP micro/millifluidic bioreactor for long-term maintenance of retinal organoids (RtOgs) [48]. Using SLA, they created a fast PDMS casting mould with integrated high structures, allowing for long-term pumping-based organoid differentiation. This micro/millifluidic system eliminated the need for macro-scale culture and manual labour, enhancing consistency of nutrition supply and fluid stability without subjecting the organoids to high shear stress. Additionally, the system's compatibility with multiphoton imaging and fluorescence microscopy facilitated observation and analysis. The vascularization of pluripotent stem cell (PSC)-derived organoids is crucial for their development, as adequate blood supply is essential for proper organogenesis. 3DPμFD have emerged as a critical enabling technology for organoid vascularization due to their easy fabrication and flexible configuration [49]. Ranga et al. devised a method to generate neurovascular organoids from human pluripotent stem cell lineages [50]. Through in vitro vascular and neural differentiation from pluripotent stem cells, they established a 3DP chip with a central organoid chamber and a flanking channel containing differentiated endothelial cells and pericytes. This configuration facilitated on-chip angiogenic sprouting toward the cerebral organoid, resulting in significant differences in protein expression patterns compared to non-vascularized brain organoids. Lee et al. developed a 3DP micro physiological analysis system for investigating immune-driven brain aging effects using human brain organoids [51]. This system allowed for studying organoid-monocyte interactions with advantages such as online perfusion, blood vessel mimicking, culture standardization, and compatibility with standard liquid manipulation. Using an SLA printer, they fabricated a hollow meshed tubular scaffold and two medium reservoirs within the system. By analysing the interaction between aged monocytes and brain organoids, they revealed specific proinflammatory cytokine secretion pathways, suggesting the contribution of aged peripheral immune cells to brain degeneration.

# 3 RESEARCH METHODOLOGY

The major goal of this study, is to develop an efficient workflow and investigate the viability of using 3D printing techniques to fabricate microfluidic devices, assisting the laboratories towards custom made microfluidics fabrication for potential use in the field of biomedical research. The use of microfluidic devices in biomedical research has attracted substantial attention because to its potential to revolutionize numerous analytical and diagnostic procedures. In this work, we will investigate and evaluate AM technology for the design and production of microfluidic devices. A custom-made triple syringe pump was designed and constructed, to enable accurate and regulated fluid flow within the microchannels. A cost-effective, entry-level 3D printer, Creality Ender 3, was used to collect all the important components for the syringe pump, including an LCD screen, motherboard, power supply, and stepper motor, demonstrating a novel and cost-effective technique. The microfluidic devices were designed and then 3DP using a commercial LCD 3D printer (Phrozen 4K) and a Prima Creator Crystal Clear resin. A detailed printability study was performed utilizing an open-source software tool (UVTools) specializing in determining optimal process parameters for open resin 3D printers to guarantee successful 3D printing of microfluidic devices.

## 3.1 CUSTOM-MADE SYRINGE PUMP FOR FLUID FLOW SUPPLY

Syringe pumps are widely used in various fields, including physics, flow chemistry, microfluidics, biology, and microscopy. However, their high cost and limited automation capabilities have led to a shift towards Do-it-Yourself (DIY) approaches. Many DIY pumps have been published, using stepper motors and leadscrews to translate rotational motion to linear motion. DIY open-source syringe pumps have found numerous applications including bioprinting. The idea and implementation of converting the Ender 3 into syringe pumps, was first introduced by Baas, S., & Saggiomo, V. [52]. Based on their work, in this study, a triple syringe pump was designed and constructed (Figure 3.1.a). One of the main advantages of this approach is the avoidance of complex Arduino or Raspberry Pi electronics and coding since the current syringe pump can be controlled directly from the LCD screen or by a simple g-code.

In this study, a Creality 42-34, z-axis stepper motor was used. The current motor has a step angle of 1.8 degrees, meaning that 200 steps are required per revolution. Also, the Ender 3, has the capability of 1/16 micro-stepping pre-installed. This feature offers the opportunity for smaller steps and more precise movement. Upon activation, the stepper motor rotates and transfers its rotation to the connected lead screw (Figure 12.(b) parts 4 and 5). Onto the lead screw, a 3D printed push block is mounted which pushes the syringes with the same speed and pressure maintaining the same flow rate in all three syringes (Figure 12.(b) part 6 and 7).

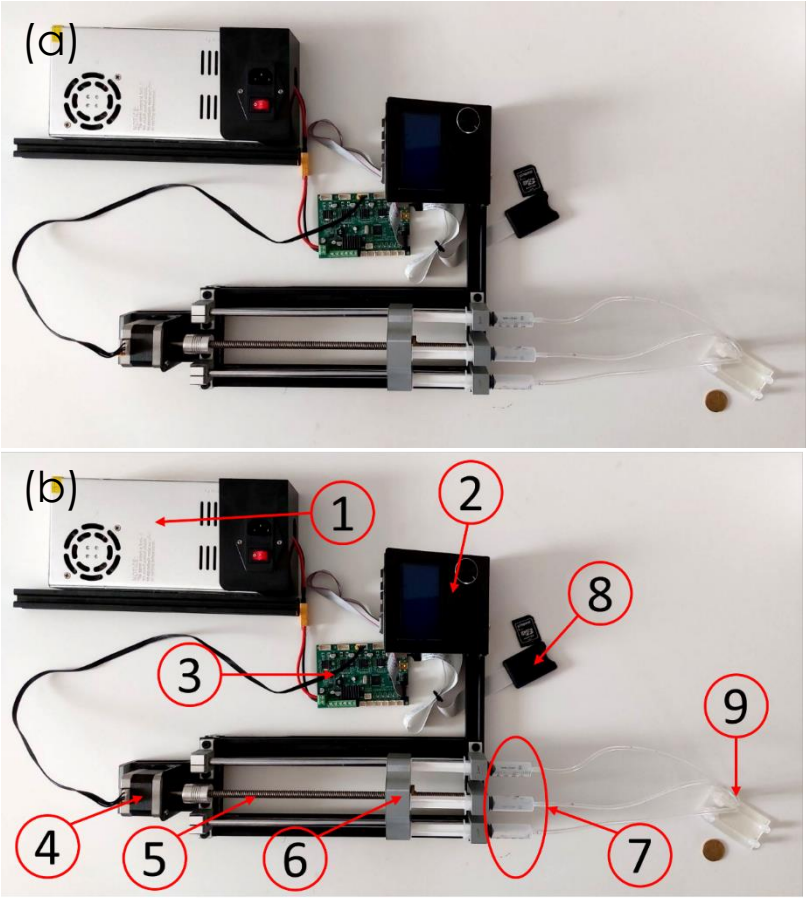


**Figure 12** (a) Top view of the fully assembled triple syringe pump and microfluidic device (50 cent coin for size reference). (b) 1. Ender 3 power supply, 2. Ender 3 LCD screen with knob controller, 3. Creality motherboard, 4. Z-axis stepper motor, 5. Z-axis lead screw, 6.3D printed push block, 7. 5ml syringes (x3 items), 8. Micro SD card extension cable (optional) and 9. microfluidic device.

To translate the rotational movement of the stepper motor into a linear movement, it is essential to calculate how many steps are required to move the push block 1mm forward. For this, one needs to know lead screw pitch, which is defined as the distance between two consecutive picks. In case of an Ender 3, the z axis integrates a triangular M5x0.8 leadscrew, meaning that the diameter is 5mm while the pitch is 0.8mm. Thus, the push block moves 1mm forward when it completes 4000 steps (eq. 3.1).

$$\frac{Steps}{mm} = \frac{steps\ per\ revolution * microstep}{lead\ screw\ pitch} = \frac{\frac{360°}{1.8°} * 16\ steps}{0.8\ mm} = 4000 \quad (3.1)$$

Since the use of a syringe pump is to dispense liquids in a controllable manner, it is essential the eq. (3.1) to be converted from *steps/mm* into *steps/mL*. Knowing the total syringe volume (*V*), the piston's inner diameter (*d*) and the inner syringe length, the total linear distance that the push block needs to travel for 1ml to be dispensed from the syringe, can be calculated as follows. 1ml equals 1cm$^3$, dividing this by the piston's area (cm$^2$), we can calculate the linear syringe travel. Since the steps/mm was found to be 4000, the steps/mL can be found when dividing the linear syringe travel with the 4000. The syringes used in this study had 5 ml volume and inner diameter of 12.3mm giving 33663 steps/ml. To move the syringe pump in a controllable and user-friendly manner, a simple g-code file needs to be created. Here is the code for dispensing 1ml under a constant fluid flow of 1ml/min:

**M**92 **Z**33663; setting up the proper steps/ml for a 5ml syringe
**M**302 **S**0; Initiate process bypassing temperature check
**M**211 **S**0 ;Disable endstop switch
**G**91; Relative position
**G**1 **Z**1 **F**1; Dispense 1ml of liquid under constant flow rate of 1ml/min

The M92 command at the start of the g-code set the proper steps required for moving the push block 1 mm. The M302 S0 enables the motors movement without checking for the temperature hot end. M211 S0 disables the endstop switches as none of them are used. G91 denotes the relative position of the push block while the G1 Z1 F1 command, moves the push block 1mm forward at a flow rate of 1ml/min.

The above g-code can be either saved and executed from a microSD card or by connecting the syringe pump with a computer/laptop running ProntFace which is a free, open-source software for 3D printers and CNC control. Bill of Materials and detailed view of the syringe pump in the APPENDIX section 8.1.

## 3.2 MATERIALS AND PRINTABILITY ASSESMENT

The current section focuses on the assessment of materials printability and the optimization of the 3D printing process for fabricating microfluidic devices. Specifically, photosensitive Crystal-Clear resin is employed due to its excellent optical transparency and compatibility with microfluidic applications. The VPP 3D printer, Phrozen Sonic 4k, is utilized for its high-resolution capabilities and suitability for fabricating intricate 3D structures with a variety of photosensitive resins at 405nm. To determine the optimum

printing process parameters, UVtools, an open-source software, is employed. UVtools offers advanced process optimization functions, enabling the identification of the most suitable printing settings for each resin and specific purpose.

The primary objective of this study is to produce microfluidic devices with exceptional fidelity to CAD models, ensuring precise replication of complex microfluidic features. By optimizing the printing process parameters using UVtools, we aim to achieve high-resolution printing, smooth surfaces, and reliable repeatability. The successful implementation of this approach has the potential to democratize the fabrication of microfluidics, enabling researchers to efficiently fabricate functional microfluidic devices for diverse applications ranging from biological analysis to point-of-care diagnostics.

**Photosensitive Resin Material**

Primacreator value Uv/DLP Crystal Clear resin was used towards the fabrication of 3DPμFD with high transparency, low shrinkage after post treatment and no yellowing after Uv curing. It is optimized to absorb Uv/vis between 395 to 405nm within 4 to 8 seconds per layer. Table 5 shows the indicative chemical composition of the photosensitive resin used, Information availability (Prima Creator)

**Table 6** Crystal Clear Resin indicative composition

| Name of substance | Identifier | Wt% |
|---|---|---|
| Esterification products of acrylic acid with reaction products of 2,2-dimethylpropane-1,3-diol and methyloxirane | CAS No 84170-74-1 | 25 – < 50 |
| 4,4'-Isopropylidenediphenol, oligomeric reaction products with 1-chloro-2,3-epoxypropane, esters with acrylic acid | CAS No 55818-57-0 | 25 – < 50 |
| (5-ethyl-1,3-dioxan-5-yl)methyl acrylate | CAS No 66492-51-1 | 10 – < 25 |
| Ethyl phenyl(2,4,6-trimethylbenzoyl)phosphinate | CAS No 84434-11-7 | 5 – < 10 |
| Titanium dioxide | CAS No 13463-67-7 | < 2 |

**VPP 3D Printer**

In this work, a Phrozen Sonic 4k resin LCD 3D printer (Figure 13), was utilized for its high-resolution capabilities and suitability for fabricating intricate 3D structures with a variety of photosensitive resins at 405nm. The Phrozen Sonic 4K 3D printer is a 3D printer that is designed for high-resolution and precision printing. It uses an LCD-based masking approach to solidify liquid resin layer by layer, yielding to detailed 3D objects. The Phrozen Sonic 4K has 35 micrometer XY resolution, enabling for the fabrication of delicate features with high precision. It has a monochrome 4K LCD screen with a 6.1-inch dimension and a resolution of 3840 x 2160 pixels. The printer's light source is a high-performance paraled array 3.0 that emits at 405nm. Its Z-axis offers a layer resolution from 10-300 μm enabling the production of extremely smooth detailed prints. Both Z and XY resolution is resin-dependent and printability assessment is required.

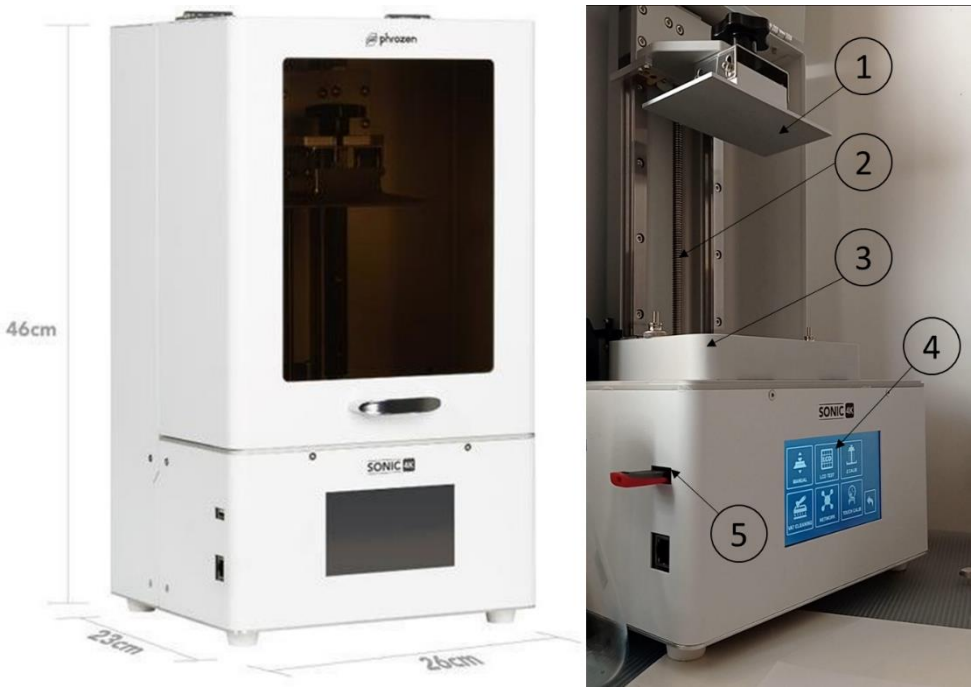


**Figure 13** (Left) The exterior design of Phrozen Sonic 4K (Right) The interior of the 3D printer when 1. Is the build plate platform, 2. Lead screw, 3. Resin vat, 4. LCD touch screen, 5. USB stick.

**Washing and Light Curing Station**

Apart from the photosensitive resin and the 3D printer that are required to produce the 3DPμFD, post process equipment is needed to achieve optimal surface quality, mechanical stability, and dimensional accuracy. Once the printing process has been completed, the printed objects are detached from the surface of the metallic build plate platform and rinsed with IPA. The excess uncured resin is removed, eliminating the residual stickiness, and enhancing the overall surface cleanliness of the 3D printed object. After cleaning with IPA, the 3D printed object undergoes further light exposure inside a Uv/vis chamber utilizing a light source with the same or even better characteristics from the first one ensuring complete cross-linking of the resin residue. The addition uv/vis exposure facilitates the conversion of any remaining uncured resin into a fully cured state, resulting in improved strength, stability, and chemical resistance of the device. However, the time required for a 3D printed object to be further cured is resin-dependent and could have either a positive or negative effect on the final properties. Thus, proper post-cured experimentation is needed. A comprehensive post treatment guide is usually available from the resin manufacturer. Although deviations from the nominal suggestions are quite often. Slight modifications of the washing and light curing protocols are required to properly post treat the 3DPμFD. Firstly, the 3DPμFD are rinsed into IPA under continuous magnetic or manual stirring for 5 minutes. Using a syringe filled with IPA and the proper tubing connection, the excess resin trapped inside the microfluidics channels, is forced to be removed preventing unwanted light curing and channels clogging. These steps could be repeated as many times as is necessary. Compressed air can further assist in unclogging the microfluidic channels. Post curing in uv/vis chamber can further enhance the quality of the final part, however, it can compromise the transparency of the final 3DPμFD, thus post curing can be avoided if the device is properly washed out and no excess resin is evident. In this study, a magnetic stirrer, a Wanhao Boxman UV Curing Chamber, a syringe, and IPA were used to post process the 3DPμFD as described above.

**Printability Assessment**

To find the optimal printing settings for the Crystal-Clear resin, the open-source software UVtools from Tiago Conceição[4] was employed. The main advantage of UVtools is that offers the assessment of different printing process parameters simultaneously. It exports test coupons with different exposure times for bottom (initial) layers and normal (intermediate and last) layers. Each test coupon is denoted by 3 numbers in the left and right bottom corner, layer height, bottom layer and normal layer exposure time (Figure 14). Furthermore, each test coupon appears in its surface the same features (Figure 15):

An array of positive and negative pillars (pins and holes): The purpose of the pillars validation is to have an equal number of pillars on both the negative and positive sides. However, in most cases, this balance is not attained, and the smallest positive pillar will

[4] https://github.com/sn4k3/UVtools

not print due to its thin wall. Therefore, it is recommended to validate this test last. Overexposure may allow the smallest pillar to be printed, but it does not necessarily mean that the corresponding timing should be chosen. This test also provides information about the minimal area that the printer can successfully print under those specific conditions. (A similar situation can occur with zebra bars.)

Zebra bars: During the assessment of zebra bars, underexposure is indicated when numerous lines are absent, the lines are reduced or deformed, and there is notable gap between them or between the bars and the frame. Furthermore, underexposure could be implied if the number of positive bars is less than the number of negative bars. On the other hand, overexposure is indicated if the lines have extended and overlap with adjoining bars and when the number of positive bars exceeds the number of negative bars.

Text: Underexposure is indicated if the text is incomplete, lacking components, or seems excessively thin. Overexposure is indicated if the writing is bold and thick, with certain sections seeming merged or creating a white blob.

Bullseye: Underexposure is denoted when features show a noticeable shrinkage, damage, or absence, resulting in increased spacing between concentric circles. On the contrary, overexposure causes the features to appear bold and thick with some elements being merged together or forming a white blob.

Counter Triangles: Underexposure is evident when the tips of the four triangles are far away from each other while overexposure can be observed when the tips are connected forming a white blob.

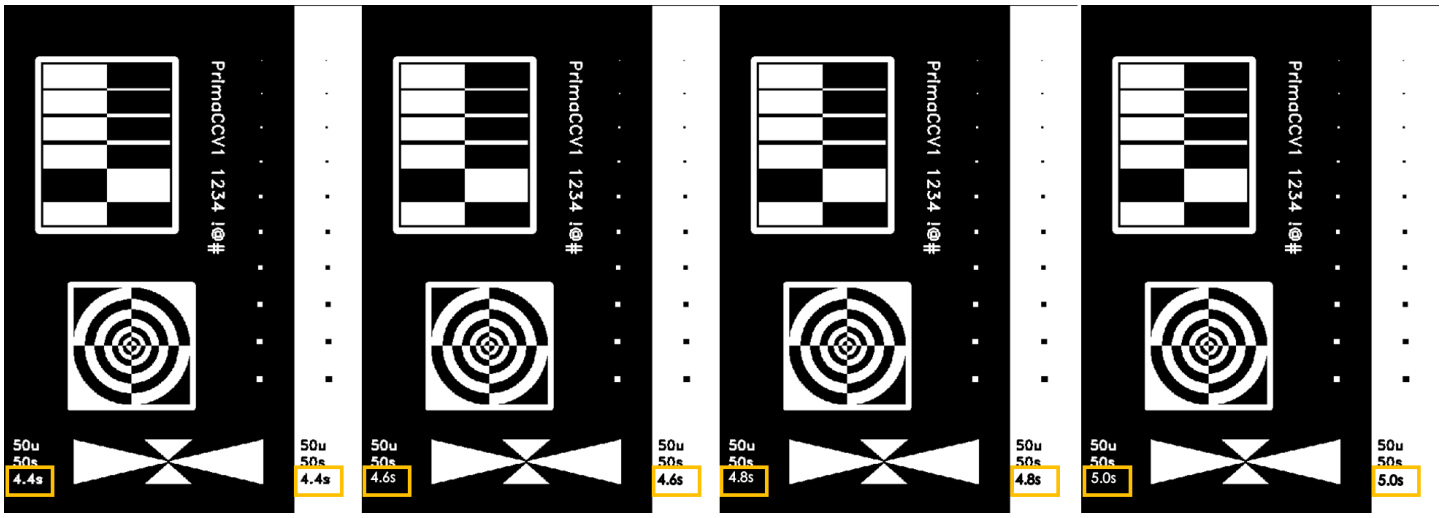


**Figure 14** Printability test coupons generated via UVtools. Within the yellow boxes the different normal time exposure to properly investigate the optimum light exposure time. The first number denotes the layer hight while the second one indicates the light exposure time for the first layers.

Black areas are masked and no Uv light penetrates while white areas denote the unmasked pixels allowing for the UV to pass towards the photosensitive resin. This extremely useful feature is currently excluded from all the available VPP slicers. Equipped with a variety of 3D printing calibrations assessments, focused on VPP 3D printing, the printability assessment of a new resin can be lowered down to a few hours rather than days of testing each parameter at once.

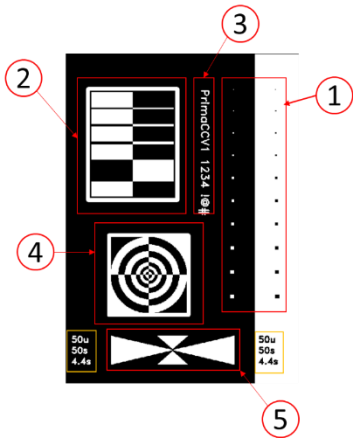


**Figure 15** UVtools printability test coupon 1. Positive and negative pillars 2. Zebra bars 3. Text 4. Bullseye 5. Counter Triangles. The information within the yellow box is unique for each test.

# 4 RESEARCH FINDINGS/RESULTS

## 4.1 PRINTING PROCESS OPTIMIZATION

As it was mentioned before, UVtools was employed for printing process optimization towards the fabrication of microfluidic devices. The proper light exposure time for the Crystal-Clear Resin was found after four iterations (Table *7*). The tested coupons printed in Phrozen Sonic 4K, parallel to the built platform and then washed with IPA for 5 minutes, left from completely drying and then post cured for another 5 minutes inside the Wanhao Boxman UV Curing Chamber.

**Table 7** Uv/vis exposure time assessment for the normal layers. Color gradient coding denotes the outcomes from the different exposure times used. Red under exposure and green the optimum time exposure window.

| a/a | Layer Height (μm) | Bottom exposure (s) | Bottom layer number | Normal Exposure (s) |
|---|---|---|---|---|
| 1 | 50 | 50 | 8 | 2.0 to 3.2 |
| 2 | | | | 3.0 to 4.4 |
| 3 | | | | 4.0 to 5.0 |
| 4 | | | | 4.4 to 5.0 |

Figure 4.1 shows the results of the time exposure optimization of the normal layers. Each test was conducted with 50μm layer height, 8 bottom layers and 50s bottom layers exposure. By increasing the light exposure of the bottom layers, the adhesion of the printed test coupons increases while overexposure occurs. This leads to a thicker base with a strong grip to the built plate platform. Here, to evaluate the exposure time of the normal layers, a bottom layer exposure of 50s ensures the successful printing of the base with the perfect possible adhesion without dramatically overexposure the resin. The optimization of the bottom exposure is known as the *elephant foot assessment*. Four different normal exposure time frames were used to proper investigate the printability of the Crystal-Clear resin with a constant time step of 0.2s. Initially, a time range of normal layer exposure between 2.0 to 3.2 seconds was used and 7 different 3D printed test coupons produced with unique results (Figure 16.a and b). The first experiment yielded to underexposed samples with either insufficient resin solidification or even damaged surfaces. During the second experiment 8 3D printed coupons were produced within a time range between 3.0 and 4.4s (Figure 16.c and d). Here, time exposures of 4.2 and 4.4 presented improved printing results and a new test within the range of 4.0 to 5.0 was initiated (Figure 16.e and f). More sufficient printing results started to appear between 4.6 and 4.8 seconds while 5.0s produces the best printed

features. Repeating the printing process one more time within the time range of 4.4 and 5.0 seconds, the optimum exposure time lies between 4.8 and 5.0 seconds. Thus, 4.9 seconds was chosen. To eliminate the *elephant foot* effect, a bottom exposure time to 30 seconds was found to be ideal. Using a Leica S9D stereoscope[5], detailed visual inspection of the most promising 3D printed outcomes was performed (Figure 17). Although the majority of the surface features have been printed, in 4.4s exposure time, some of the zebra bars appear to be absent, damaged and deformed. The bullseye shape are poorly formed and large gaps appear between the arcs while the counter triangles are partially connected. No text was printed. Under exposure for 4.6s, all the surface features are well printed with minor artifacts mainly in the zebra bars and in the arcs of the bullseye. Triangles start to separate from each other and resemblance the nominal structure. Text was sufficiently printed, and it is readable. Increasing even more the exposure time, the results obtained with 4.8s are even better than the previous ones. Zebra bars are well printed sharing tinny connections. Counter Triangle presents a larger and more defined gap. Text presents improved quality. 5.0 s exposure presents the best overall quality. However, in order to prevent internal clogging while printing microfluidics, the exposure time was set slightly below the optimum exposure time, thus 4.9s was chosen.


**Figure 16** Time exposure investigation towards the optimum normal layer printing result. (a and b) show extreme underexposure while (c and d) presents sufficient outcomes. (e and f) present promising printing results with (g and h) indicates right exposure time between 4.8 and 5.0 seconds. Thus 4.9 was chosen. (i and j) show the object configuration from the interface from the UVtools software.

[5] Located in BIOG3D premises.

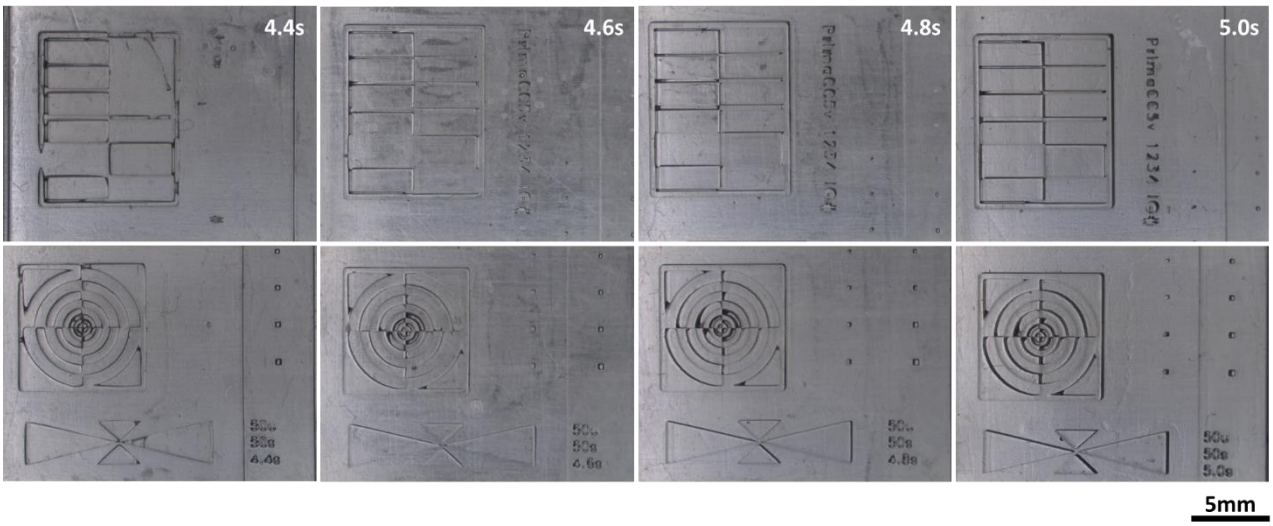


**Figure 17** Detailed view of the printability assessment test coupons utilizing normal layer exposure times from 4.4 to 5.0 seconds with a constant step of 0.2s.

## 4.2 MICROFLUIDICS FABRICATION

Once the optimized 3D printing parameters have been investigated and established, the next step is to proceed with the fabrication of the microfluidic device. To further validate the printing parameters for microchannels fabrication, a square block with four open channels 0.5 mm depth and with different widths, was designed and 3D printed. The 3D printing process parameters were obtained from the UVtools and used in Chitubox. Chitubox, is a free slicing software for open-LCD/DLP 3D printers. In the APPENDIX section 7.2, more detailed information about the Chitubox settings is provided. The square block printed parallel to the build platform. Table 8 shows the nominal value and the measured value of the width of the four open channels. Figure 4.3 shows a top view of the microchannels under the Leica S9D stereoscope. The measured distances present no significant deviations from the nominal values proofing the reliability of the manufacturing process (Figure 18.F)

**Table 8** Comparison between nominal and experimental values of channel widths for 3D printing process parameters validation.

| Channels | Nominal Width (mm) | Printed Width (mm) |
|---|---|---|
| 1 | 0.05 | 0.053 |
| 2 | 0.1 | 0.134 |
| 3 | 0.5 | 0.5 |
| 4 | 2 | 1.985 |

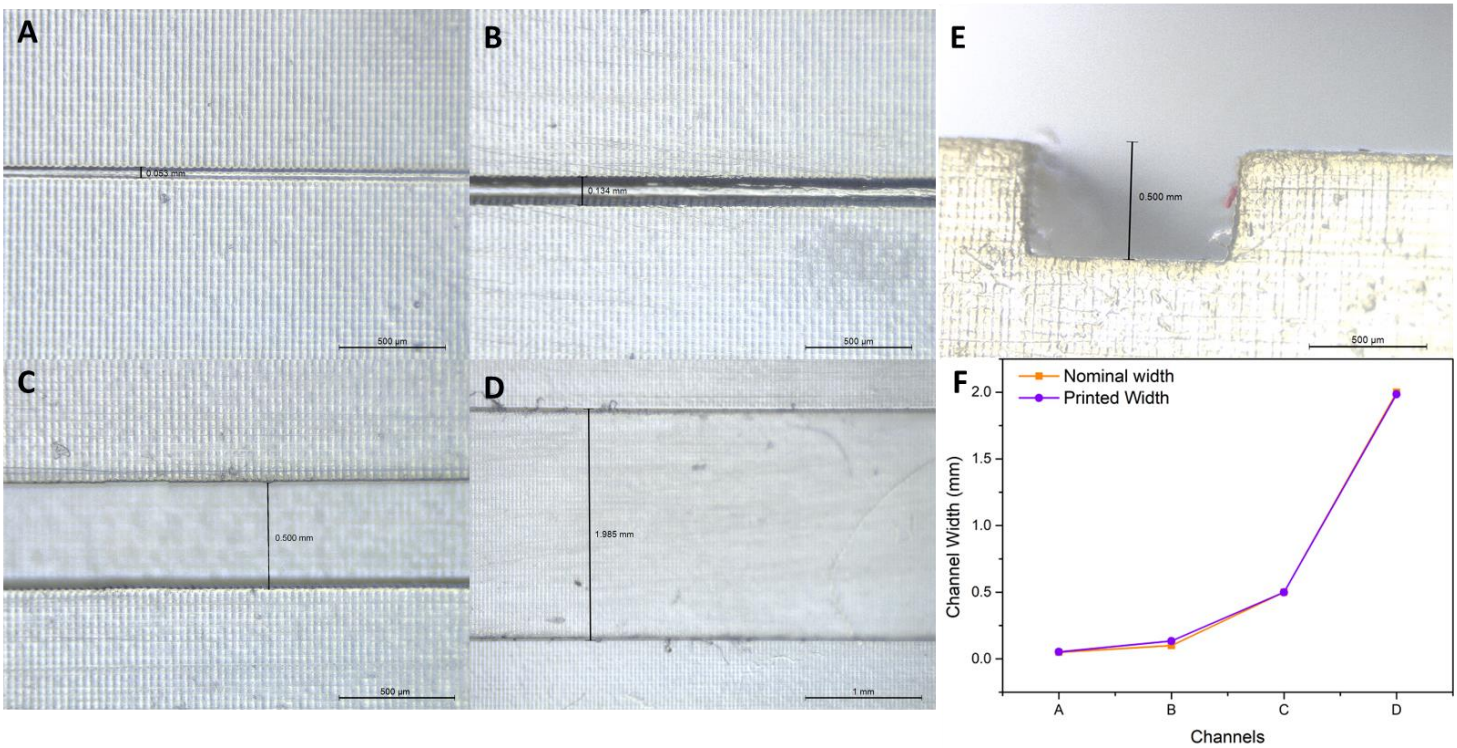


**Figure 18** (A-D) 3D printed open microfluidic channels towards the validation of the optimized 3D printing process parameters. (E) Channel cross section of 500µm depth. Scalebars have 500µm length. (F) Comparative graph showing that the measured values are in a great agreement with the nominal dimensions

In the framework of this study, a microfluidic device with two droplet generators was designed and 3D printed. Droplet microfluidics is a technique for manipulating discrete fluid volumes with immiscible phases [53]. It has been used in multiple biomedical applications including but not limited to single-cell analysis, drug synthesis, drug delivery, protein analysis, DNA and genomics [53-55]. Such devices offer the capability of producing size-controlled particles which can be used as drug delivery systems [56]. Droplet microfluidics are commonly used to produce micro-carriers combining different pharmaceutical compounds with controllable release [57]. Janus droplets are droplets consisting of two distinct regions with different chemical or physical properties [58]. Their name is derived from the Roman God Janus. According to Roman mythology, Janus, among others, he was the God of beginnings, transitions, time, duality, and endings. Thus, he had two faces looking in opposite ways, one towards the past and one towards the future [59]. Microfluidics Janus droplets generators are devices that exploit the laminar co-flow of two fluids that are forced to exit from an orifice, without previously being mixed, meeting a continuum phase of immiscible solvents [60]. Such droplets can be used for drug synthesis while encapsulating two different reagents in the two separated regions within a single droplet (Figure 19) [61]. Considering the importance of such devices, in this study, a Janus droplet and a Double T- Junction microfluidic generators were designed in a single microfluidic device as a demonstrator (Figure 20).

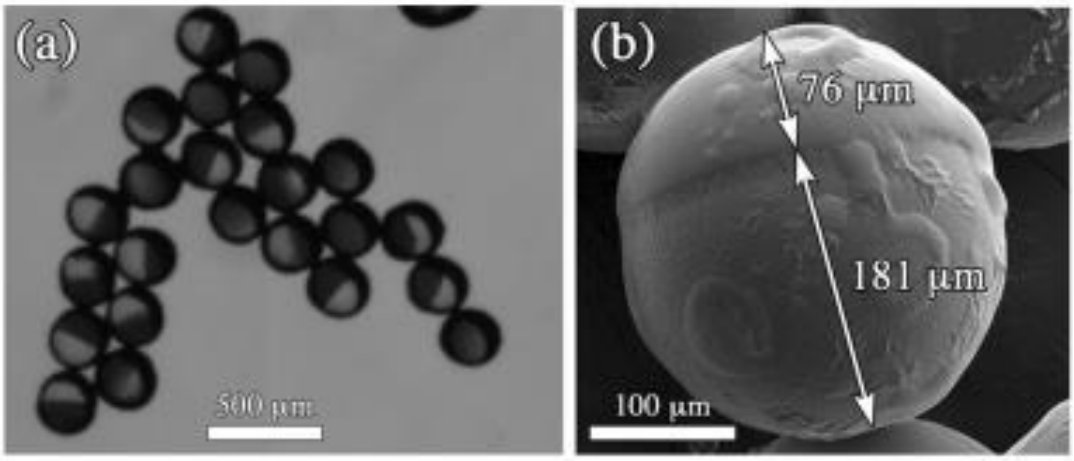


**Figure 19** (a) Janus particles under optical microscope and (b) SEM image of the Janus particles showing the two distinct compartments containing two different active pharmaceutical ingredients [61].

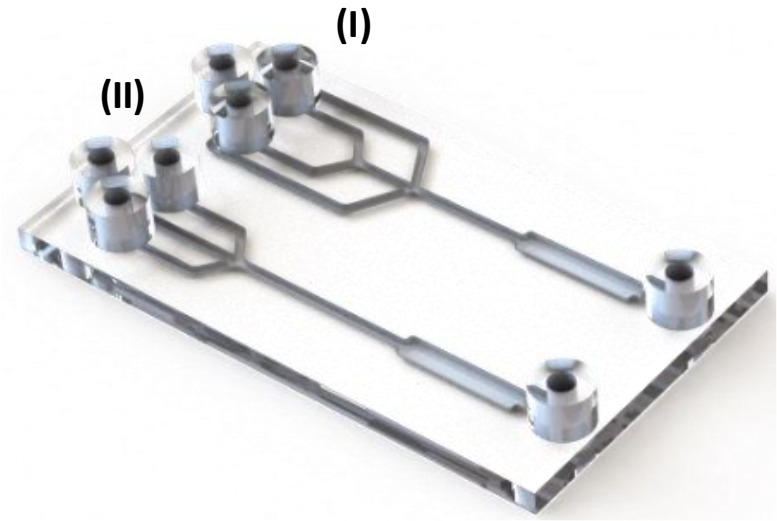


**Figure 20** A photorealistic representation of the microfluidic device which includes two droplet generators. (I) The first droplet generator has been designed to produce Janus droplets. At a junction, two parallel streams co-emulsify into a continuous phase while retaining two discrete domains. (II) Double T- Junction droplet generator.

Both droplet generators are designed with the intention to be used in drug synthesis and analysis. However, the analysis of the generated droplets is not part of this study. The current microfluidics consist of three inlets, one outlet, a droplet formation region and a droplet compartment for droplet collection and analysis (possible by employing spectral assessment). The Janus droplet generator (Figure 20 (I)) form biphasic droplets in laminar flow regime. Two miscible streams are guided towards the orifice in parallel flows inside the microchannel and emulsified into droplets at the orifice when they meet a third continuous media which induces a drag force on the co-flow stream. Although vigorous rotational flows can be generated as a result of external shear forces during the formation of droplets at the orifice, the device's centerline symmetry produces a rotational flow

confined within its own hemispherical domain to produce twin circulatory flows with negligible convective mixing. Hence, the produced Janus droplets preserve their compartmentalization as they flow within a symmetric microfluidic channel. Tortuous channels or non-uniform density among the droplets can induce the internal mixing [62]. The second droplet generator is a Double T- Junction microfluidic system in which consecutive droplets, from one aqueous solution at the time, are formed.

To maximize the high throughput of the droplet formation, larger channels can be used allowing more and larger droplets to pass through. However, by increasing the channel width and depth, the dispersion and stability of the droplets are compromised [63]. The microfluidic devices designed in this study, have 1mm width and 0.5mm depth (Figure 22).

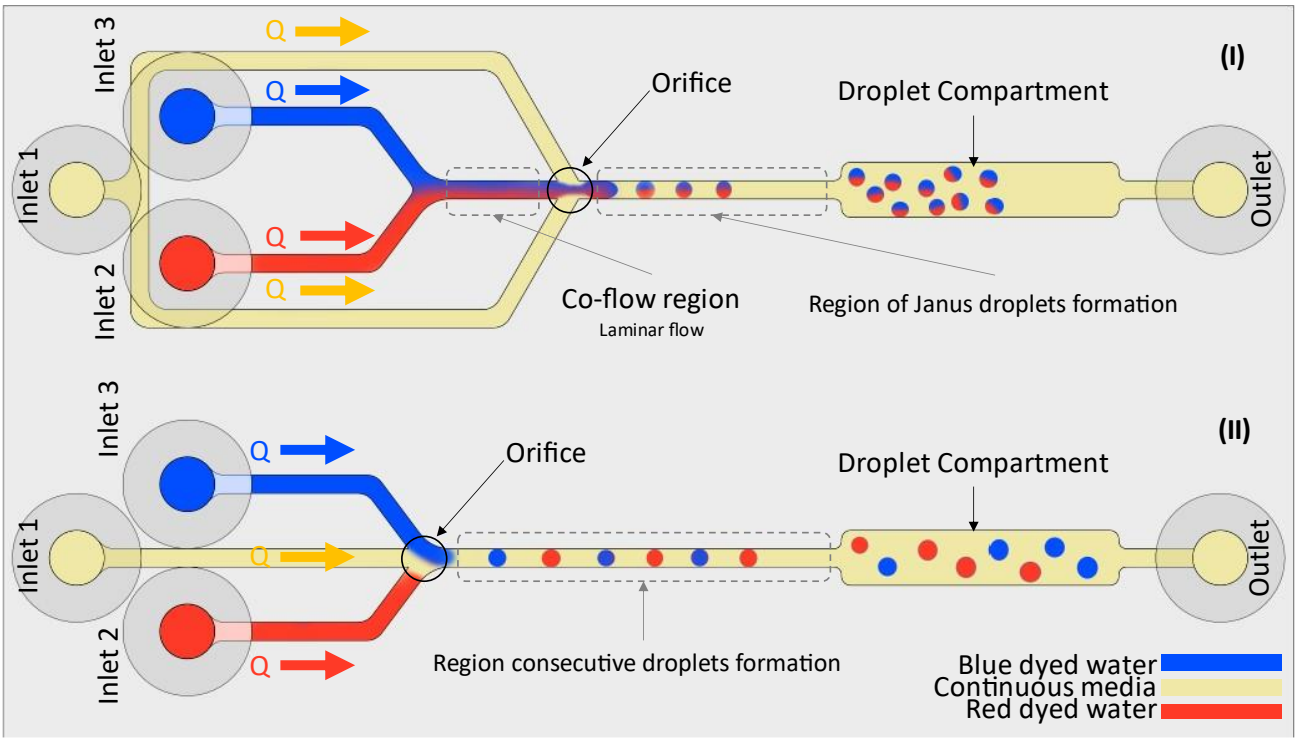


**Figure 21** Schematic representation of the fluid flow inside the microfluidic devices. A continuous media (olive oil) food coloured water (blue and red) were used to validate the fluid flow of each droplet (I) Janus droplet generator and (II) Double T- Junction droplet generator. The triple syringe pump provides a constant fluid flow, denoted with Q.

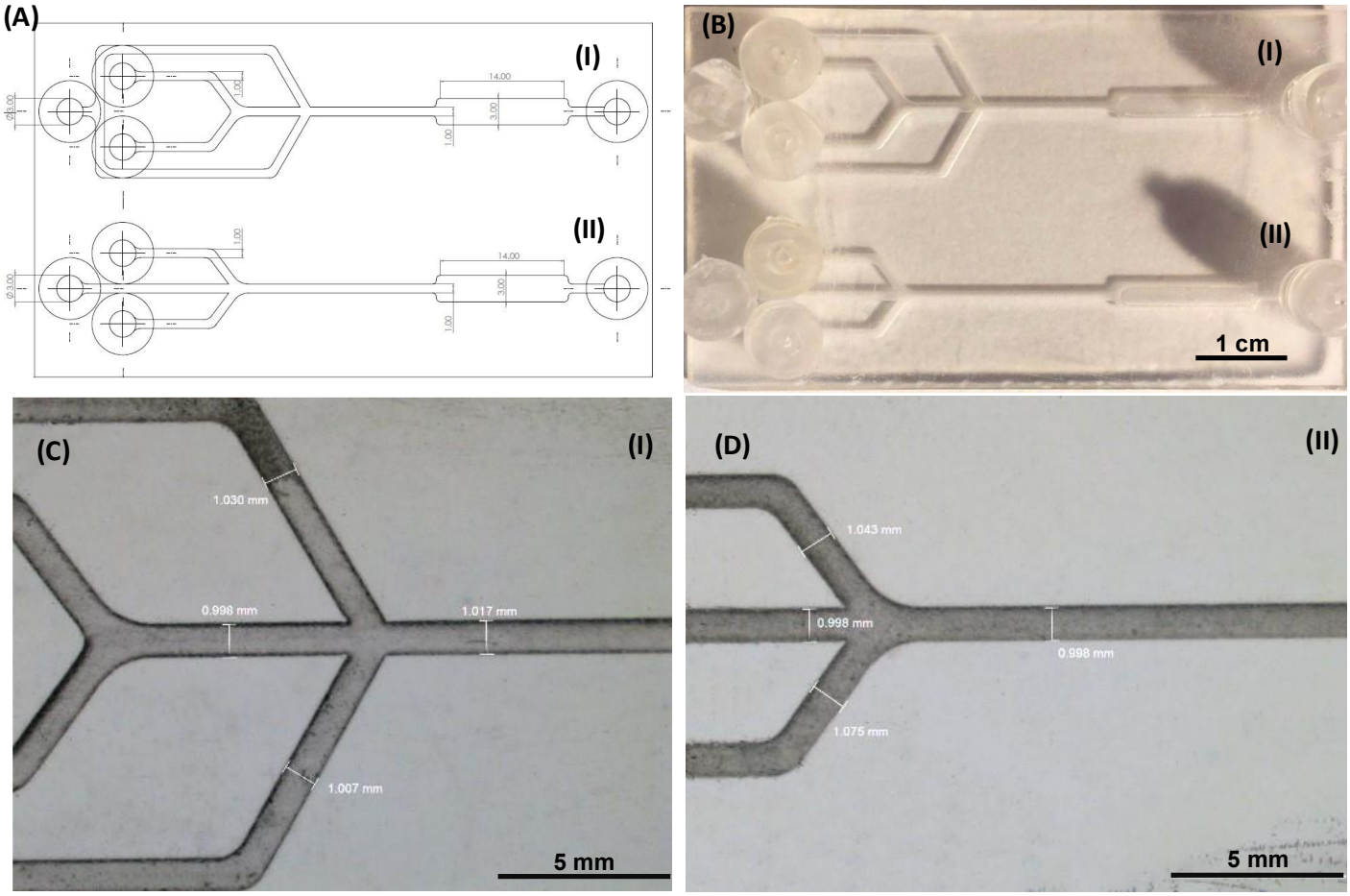


**Figure 22 (**A) Technical/Engineering drawing of a microfluidic device with two droplet generators and their dimensions. Channels are 1mm thick and 0.5mm deep. Droplet compartments are 3mm thick and 14mm long. (B) 3D printed microfluidic device with the two droplet generators successfully formed. (C and D) Validation of the microfluidics dimensions under the Leica S9D stereoscope. (I) Janus droplet generator and (II) Double T- Junction droplet generator.

The microfluidic device was designed utilizing CAD software, exported into STL file and imported into the Chitubox slicer for gcode generation. The printing process parameters are based on the optimized settings found above. Detailed explanation regarding the process parameters in Chitubox can be found in APPENDIX section 8.2. The microfluidic device was printed with the flat, bottom face in contact with the build plate of the Phrozen Sonic 4K. After printing, the device was removed from the build plate and immersed in IPA bath for 5 minutes under constant stirring. Using a syringe filled with IPA the microchannels were flashed to clean the trapped resin. When cleaning finished, the microfluidic device underwent post cure for 5 minutes for further solidification towards a more mechanical and chemical stable result. Using the Crystal-Clear Resin from Primacreator, the final device presents adequate transparency and thus no need for surface post treatment required. However, if the surface transparency is insufficient, post process using consecutive sanding from 100 to 2000 grit can be employed with as many iterations as needed. After that, spraying with clear acryl can further enhance the transparency of the final device with inlets and outlets sealed.

# 4.3 FLUID FLOW ASSESSMENT

To validate the fluid flow inside droplet generators, the DIY syringe pump was connected with the microfluidic device using 3D printed tube connectors 3x2.85 mm (Figure 23) and silicon tubes of 3mm inner and 4mm outer diameter. Two syringes filled with dyed water (red and blue) and one filed with olive oil, were inserted into their respective housings (syringes with coloured water placed in the Side Rod Stops while the oil syringe was inserted into the Mid Lead Screw Housing- parts in Table 8, APPENDIX) (Figure 24). Since water and oil have opposite polarities, they offer a simple and reliable way to assess the performance of the device. By flashing the G-Code (Section 3.1), 1ml of the three fluids are introduced with the same flow rate into the microfluidic device.

**M**92 **Z**33663; setting up the proper steps/ml for a 5ml syringe.
**M**302 **S**0; Initiate process bypassing temperature check
**M**211 **S**0
**G**91; Relative position
**G**1 **Z**1 **F**1; Dispense 1ml of liquid under constant flow rate of 1ml/min.

Upon activation, no leakages, back flows, vortices, or air bubbles were observed, ensuring that the tubing connections were perfectly sealed and the design of the droplet generator ideal. Figure 25 presents the result of the fluid flow assessment towards the formation of Janus droplets. As it was described above, the two-colored water fluids co-flow without mixing since they flow at the same flow rate. After exiting for the orifice, the aqueous, polar phase meets the non-polar phase of the oil and Janus droplets are formed. As it is observed from the results, different Janus droplet sizes are formed when the flow rate changes. At 5ml/min flow rate, small Janus bi-phasic droplets are formed while at 1ml/min the produced Janus particles are bigger (Figure 25 b and c). The same applies to the Double T-Junction when large, elongated droplets are formed in low flow rates 1ml/min while 5ml/min produces smaller more spherical droplets. At low flow rates, droplet merging is possible due to the increased number of droplets within the droplet compartment (Figure 26).

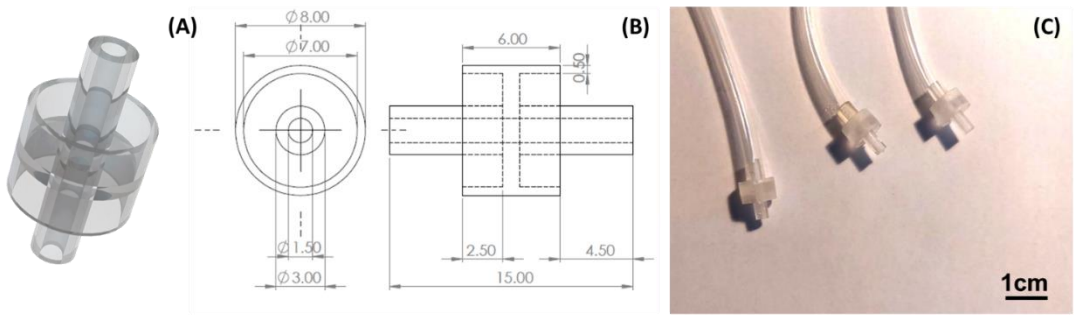


**Figure 23** (A) Photorealistic representation of the inlet/outlet connector (B) Technical/Engineering drawing of the microfluidic connector (C) Tubing assembly

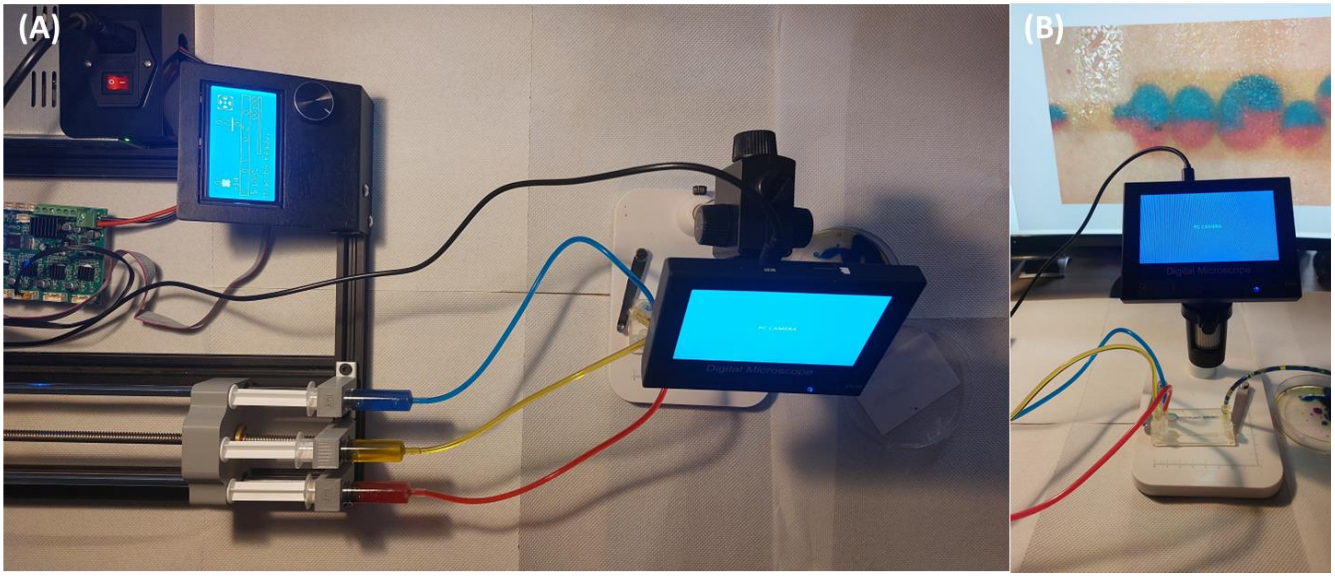


**Figure 24** (A) Operational set up of DIY syringe pump and microfluidic device. (B) A portable, digital and low-cost microscope (ANDOWL XQ-XW01, China) was utilized to assess the fluid flow during operation

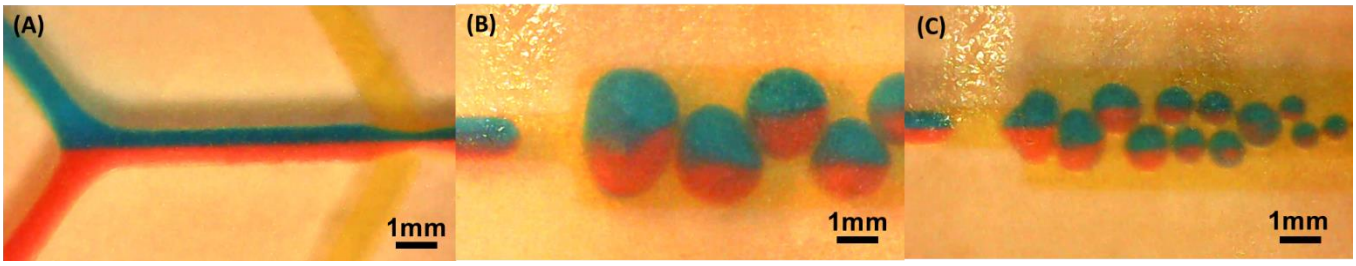


**Figure 25** Fluid flow assessment of Janus droplet generator. Droplets are spherical with distinct immiscible compartments. (A) Laminar co-flow of coloured fluids before exiting from the orifice. (B) Big Janus particle formed at flow rate of 1ml/min (C) Smaller Janus particles at 5ml/min

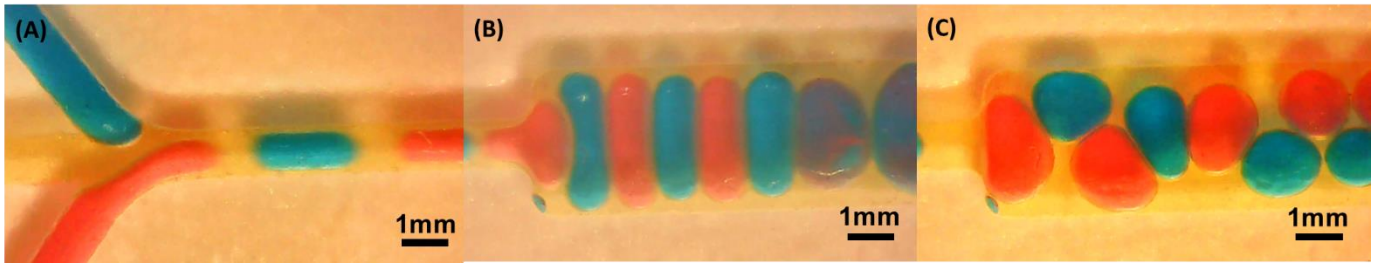


**Figure 26** Fluid flow assessment of Double T- Junction droplet generator. Droplets are either squeezed and elongated or spherical. (A) Consecutive droplet formation (B) Squeezed and elongated droplets formed at flow rate of 1ml/min. Due to the small droplet compartment and the high concentration of droplets number, droplet merging is possible (C) Droplets are formed when higher flow rate is applied, 5ml/min.

# 5 DISCUSSION AND ANALYSIS

The current master's thesis titled "3D printing of polymeric microfluidics devices" investigates the design and assessment of microfluidics devices utilizing the Vat Photopolymerization (VPP) technique. More specifically LCD technique. The study was conducted as part of the interdisciplinary master's program of Biomedical Engineering, organized by the University of Crete, the Technical University of Crete, and the Foundation for Research and Technology Hellas.

VPP provides the ability to fabricate, layer-by-layer, complex microfluidic devices with great accuracy without the need of a clean room equipment. By utilizing VPP, this study aims to provide a comprehensive workflow towards the design and production of 3D printing microfluidic devices for biomedical applications. To evaluate the fluid flow within the microfluidic devices, a custom-made (DIY) triple syringe pump was designed and fabricated. The pump was created using components readily available in an affordable 3D printer (Creality Ender 3), ensuring a cost-effective approach to the experimental setup.

The main focus of this study was placed on biphasic droplet generation, known as Janus droplets, and consecutive droplet generation. By successfully fabricating microfluidic devices using VPP, this study demonstrates the feasibility for cost-effective manufacturing of intricate microfluidic devices. By employing VPP and a custom-made triple syringe pump, we successfully showcase the precise fluid flow control within the microchannels, enabling the generation of controllable droplet morphologies. The findings of this research, offer a simple and effective approach to democratize the microfluidic fabrication. The developed workflow provides a foundation for further exploration and optimization of 3D printing techniques in microfluidic device fabrication within any research lab. One of the benefits of 3D printing microfluidics is the ability to rapidly prototype and iterate designs. This allows for rapid changes and upgrades to device geometries and capabilities, allowing for the development of bespoke solutions for specific biomedical applications. While the focus of this research was on biphasic droplet creation and successive droplet generation, the principles and techniques developed can be applied to various microfluidic applications such as cell manipulation, drug delivery systems, and lab-on-a-chip devices. The ability to use 3D printing to create low-cost, custom-designed microfluidic devices has enormous potential for enhancing biomedical engineering research and applications.

# 6 CONCLUSION AND RECOMMENDATION

Conclusions:

This master dissertation focused on the 3D printing of polymeric microfluidic devices towards potential biomedical applications. The study successfully demonstrated the feasibility of utilizing VPP, for fabricating microfluidic devices. The custom-made triple syringe pump developed using components found in an affordable 3D printer (Creality Ender 3), for precise fluid flow control within the microchannels. The research findings highlight the advantages of 3D printing in microfluidics, including rapid prototyping, customization, and cost-effectiveness. The proposed workflow for 3D printing microfluidic devices, depicts the possibilities for developing tailored solutions in the field of biomedical engineering. The ability to create low-cost, custom-designed microfluidic devices within hours, holds immense potential for various applications, such as cell manipulation, drug delivery systems, and lab-on-a-chip devices.

Recommendations:

Based on the results and limitations of this study, several recommendations can be made for additional research and development. Optimization of the custom-made triple syringe pump: Further optimization and calibration of the pump design are recommended to improve flow control accuracy, reliability, and versatility. This could involve exploring alternative pump designs or incorporating advanced flow control mechanisms. Exploration of alternative 3D printing technologies and materials: While VPP offers high-resolution printing capabilities, investigating other 3D printing technologies, such as Two-photon polymerization (2PP), Femtosecond Laser Ablation, Projection micro Stereolithography could provide access to a wider range of materials and properties. Integration of functional components: Functional components within 3D printed microfluidic devices, such as sensors, electrodes, or membranes could be incorporated enhancing the capabilities of the devices. Hence, enabling more complex and integrated functionalities, opening up possibilities for advanced biosensing, cell analysis, and drug delivery applications. This approach makes the microfluidic device more complex and thus a hybrid manufacturing approach is needed. Validation and characterization of 3D printed microfluidic devices: Surface characterization using scanning electron microscopy (SEM), atomic force microscopy (AFM) and contact angle assessment, would be adequate techniques to validate and optimize the 3DP microchannels' surface properties. Also, evaluating factors such as fluid flow dynamics utilizing sensors and/or computational fluid dynamics (CFD) simulation as well as droplet generation control with a highspeed camera for particle image velocimetry, would conclude the validation assessment of the produced devices.

# REFERENCES

[1] Information, Reed Business (3 October 1974). "Ariadne". New Scientist. 64 (917): 80. ISSN 0262-4079.

[2] Kodama, H. (1981). Automatic method for fabricating a three-dimensional plastic model with photo-hardening polymer. Review of scientific instruments, 52(11), 1770-1773.

[3] https://patents.google.com/patent/US4575330

[4] https://all3dp.com/2/history-of-3d-printing-when-was-3d-printing-invented/

[5] https://www.pai-labs.com/blog/3d-printing-deep-dive-part-1

[6]http://techcrunch.com/2016/05/15/how-expiring-patents-are-ushering-in-the-next-generation-of-3d-printing/

[7] https://patents.google.com/patent/DE19649865C1/en

[8] Schittecatte, L., Geertsen, V., Bonamy, D., Nguyen, T., & Guenoun, P. (2023). From resin formulation and process parameters to the final mechanical properties of 3D printed acrylate materials. MRS Communications, 1-21.

[9] Jordan, John. (2019). 3D Printing.

[10] Bagheri, A., & Jin, J. (2019). Photopolymerization in 3D printing. ACS Applied Polymer Materials, 1(4), 593-611.

[11] Bao, Y. (2022). Recent Trends in Advanced Photoinitiators for Vat Photopolymerization 3D Printing. Macromolecular Rapid Communications, 43(14), 2200202.

[12] Rubinstein, M., & Colby, R. H. (2003). Polymer physics (Vol. 23, p. 259). New York: Oxford university press.

[13] Callister, W. D., & Rethwisch, D. G. (2007). Materials science and engineering: an introduction (Vol. 7, pp. 665-715). New York: John wiley & sons.

[14] Kumar, S., Bhushan, P., & Bhattacharya, S. (2019). Fluid transport mechanisms in paper-based microfluidic devices. Paper Microfluidics: Theory and Applications, 7-28.

[15] Kitson, P. J., Rosnes, M. H., Sans, V., Dragone, V., & Cronin, L. (2012). Configurable 3D-Printed millifluidic and microfluidic 'lab on a chip'reactionware devices. Lab on a Chip, 12(18), 3267-3271.

[16] Bishop, G. W., Satterwhite, J. E., Bhakta, S., Kadimisetty, K., Gillette, K. M., Chen, E., & Rusling, J. F. (2015). 3D-printed fluidic devices for nanoparticle preparation and flow-injection amperometry using integrated prussian blue nanoparticle-modified electrodes. Analytical chemistry, 87(10), 5437-5443.

[17] Morgan, A. J., Hidalgo San Jose, L., Jamieson, W. D., Wymant, J. M., Song, B., Stephens, P., ... & Castell, O. K. (2016). Simple and versatile 3D printed microfluidics using fused filament fabrication. PloS one, 11(4), e0152023.

[18] Li, F., Macdonald, N. P., Guijt, R. M., & Breadmore, M. C. (2017). Using printing orientation for tuning fluidic behavior in microfluidic chips made by fused deposition modeling 3D printing. Analytical chemistry, 89(23), 12805-12811.

[19] Baker, M. I., Walsh, S. P., Schwartz, Z., & Boyan, B. D. (2012). A review of polyvinyl alcohol and its uses in cartilage and orthopedic applications. Journal of Biomedical Materials Research Part B: Applied Biomaterials, 100(5), 1451-1457.

[20] Salentijn, G. I., Oomen, P. E., Grajewski, M., & Verpoorte, E. (2017). Fused deposition modeling 3D printing for (bio) analytical device fabrication: procedures, materials, and applications. Analytical chemistry, 89(13), 7053-7061.
[21] Nie, J., Gao, Q., Qiu, J. J., Sun, M., Liu, A., Shao, L., ... & He, Y. (2018). 3D printed Lego®-like modular microfluidic devices based on capillary driving. Biofabrication, 10(3), 035001.
[22] Macdonald, N. P., Cabot, J. M., Smejkal, P., Guijt, R. M., Paull, B., & Breadmore, M. C. (2017). Comparing microfluidic performance of three-dimensional (3D) printing platforms. Analytical chemistry, 89(7), 3858-3866.
[23] Bhargava, K. C., Thompson, B., & Malmstadt, N. (2014). Discrete elements for 3D microfluidics. Proceedings of the National Academy of Sciences, 111(42), 15013-15018.
[24] Shallan, A. I., Smejkal, P., Corban, M., Guijt, R. M., & Breadmore, M. C. (2014). Cost-effective three-dimensional printing of visibly transparent microchips within minutes. Analytical chemistry, 86(6), 3124-3130.
[25] Urrios, A., Parra-Cabrera, C., Bhattacharjee, N., Gonzalez-Suarez, A. M., Rigat-Brugarolas, L. G., Nallapatti, U., ... & Folch, A. (2016). 3D-printing of transparent bio-microfluidic devices in PEG-DA. Lab on a Chip, 16(12), 2287-2294.
[26] Bhattacharjee, N., Parra-Cabrera, C., Kim, Y. T., Kuo, A. P., & Folch, A. (2018). Desktop-stereolithography 3D-printing of a poly (dimethylsiloxane)-based material with sylgard-184 properties. Advanced materials, 30(22), 1800001.
[27] Zhakeyev, A., Abdulrhman, M., Zhang, Y., Li, F., Chen, G., & Marques-Hueso, J. (2023). Upconversion 3D printing enables single-immersion multi-material stereolithography. Applied Materials Today, 32, 101854.
[28] Piironen, K., Haapala, M., Talman, V., Järvinen, P., & Sikanen, T. (2020). Cell adhesion and proliferation on common 3D printing materials used in stereolithography of microfluidic devices. Lab on a Chip, 20(13), 2372-2382.
[29] Kreß, S., Schaller-Ammann, R., Feiel, J., Priedl, J., Kasper, C., & Egger, D. (2020). 3D printing of cell culture devices: Assessment and prevention of the cytotoxicity of photopolymers for stereolithography. Materials, 13(13), 3011.
[30] Knowlton, S., Yu, C. H., Ersoy, F., Emadi, S., Khademhosseini, A., & Tasoglu, S. (2016). 3D-printed microfluidic chips with patterned, cell-laden hydrogel constructs. Biofabrication, 8(2), 025019.
[31] Gross, B. C., Anderson, K. B., Meisel, J. E., McNitt, M. I., & Spence, D. M. (2015). Polymer coatings in 3D-printed fluidic device channels for improved cellular adherence prior to electrical lysis. Analytical chemistry, 87(12), 6335-6341.
[32] Lin, H., Lozito, T. P., Alexander, P. G., Gottardi, R., & Tuan, R. S. (2014). Stem cell-based microphysiological osteochondral system to model tissue response to interleukin-1β. Molecular pharmaceutics, 11(7), 2203-2212.
[33] Lembong, J., Lerman, M. J., Kingsbury, T. J., Civin, C. I., & Fisher, J. P. (2018). A fluidic culture platform for spatially patterned cell growth, differentiation, and cocultures. Tissue Engineering Part A, 24(23-24), 1715-1732.
[34] Unger, M. A., Chou, H. P., Thorsen, T., Scherer, A., & Quake, S. R. (2000). Monolithic microfabricated valves and pumps by multilayer soft lithography. science, 288(5463), 113-116.

[35] Toriello, N. M., Douglas, E. S., Thaitrong, N., Hsiao, S. C., Francis, M. B., Bertozzi, C. R., & Mathies, R. A. (2008). Integrated microfluidic bioprocessor for single-cell gene expression analysis. Proceedings of the National Academy of Sciences, 105(51), 20173-20178.
[36] Rogers, C. I., Qaderi, K., Woolley, A. T., & Nordin, G. P. (2015). 3D printed microfluidic devices with integrated valves. Biomicrofluidics, 9(1), 016501.
[37] Gong, H., Woolley, A. T., & Nordin, G. P. (2016). High density 3D printed microfluidic valves, pumps, and multiplexers. Lab on a Chip, 16(13), 2450-2458.
[38] Gong, H., Bickham, B. P., Woolley, A. T., & Nordin, G. P. (2017). Custom 3D printer and resin for 18 μm× 20 μm microfluidic flow channels. Lab on a Chip, 17(17), 2899-2909.
[39] Gong, H., Woolley, A. T., & Nordin, G. P. (2018). 3D printed high density, reversible, chip-to-chip microfluidic interconnects. Lab on a Chip, 18(4), 639-647.
[40] Sanchez Noriega, J. L., Chartrand, N. A., Valdoz, J. C., Cribbs, C. G., Jacobs, D. A., Poulson, D., ... & Nordin, G. P. (2021). Spatially and optically tailored 3D printing for highly miniaturized and integrated microfluidics. Nature Communications, 12(1), 5509.
[41] Au, A. K., Bhattacharjee, N., Horowitz, L. F., Chang, T. C., & Folch, A. (2015). 3D-printed microfluidic automation. Lab on a Chip, 15(8), 1934-1941.
[42] Chan, H. N., Shu, Y., Xiong, B., Chen, Y., Chen, Y., Tian, Q., ... & Wu, H. (2016). Simple, cost-effective 3D printed microfluidic components for disposable, point-of-care colorimetric analysis. Acs Sensors, 1(3), 227-234.
[43] Su, R., Wen, J., Su, Q., Wiederoder, M. S., Koester, S. J., Uzarski, J. R., & McAlpine, M. C. (2020). 3D printed self-supporting elastomeric structures for multifunctional microfluidics. Science advances, 6(41), eabc9846.
[44] Wang, Y. I., Abaci, H. E., & Shuler, M. L. (2017). Microfluidic blood–brain barrier model provides in vivo-like barrier properties for drug permeability screening. Biotechnology and bioengineering, 114(1), 184-194.
[45] Kajtez, J., Buchmann, S., Vasudevan, S., Birtele, M., Rocchetti, S., Pless, C. J., ... & Emnéus, J. (2020). 3D-printed soft lithography for complex compartmentalized microfluidic neural devices. Advanced Science, 7(16), 2001150.
[46] Lee, H., & Cho, D. W. (2016). One-step fabrication of an organ-on-a-chip with spatial heterogeneity using a 3D bioprinting technology. Lab on a Chip, 16(14), 2618-2625.
[47] Kang, D., Hong, G., An, S., Jang, I., Yun, W. S., Shim, J. H., & Jin, S. (2020). Bioprinting of multiscaled hepatic lobules within a highly vascularized construct. Small, 16(13), 1905505.
[48] Xue, Y., Seiler, M. J., Tang, W. C., Wang, J. Y., Delgado, J., McLelland, B. T., ... & Browne, A. W. (2021). Retinal organoids on-a-chip: A micro-millifluidic bioreactor for long-term organoid maintenance. Lab on a Chip, 21(17), 3361-3377.
[49] Homan, K. A., Gupta, N., Kroll, K. T., Kolesky, D. B., Skylar-Scott, M., Miyoshi, T., ... & Morizane, R. (2019). Flow-enhanced vascularization and maturation of kidney organoids in vitro. Nature methods, 16(3), 255-262.
[50] Salmon, I., Grebenyuk, S., Fattah, A. R. A., Rustandi, G., Pilkington, T., Verfaillie, C., & Ranga, A. (2022). Engineering neurovascular organoids with 3D printed microfluidic chips. Lab on a Chip, 22(8), 1615-1629.

[51] Ao, Z., Song, S., Tian, C., Cai, H., Li, X., Miao, Y., ... & Guo, F. (2022). Understanding Immune-Driven Brain Aging by Human Brain Organoid Microphysiological Analysis Platform. Advanced Science, 9(27), 2200475.
[52] Baas, S., & Saggiomo, V. (2021). Ender3 3D printer kit transformed into open, programmable syringe pump set. HardwareX, 10, e00219.
[53] Amirifar, L., Besanjideh, M., Nasiri, R., Shamloo, A., Nasrollahi, F., de Barros, N. R., ... & Khademhosseini, A. (2022). Droplet-based microfluidics in biomedical applications. Biofabrication, 14(2), 022001.
[54] Chen, Z., Kheiri, S., Young, E. W., & Kumacheva, E. (2022). Trends in droplet microfluidics: From droplet generation to biomedical applications. Langmuir, 38(20), 6233-6248.
[55] Liu, D., Sun, M., Zhang, J., Hu, R., Fu, W., Xuanyuan, T., & Liu, W. (2022). Single-cell droplet microfluidics for biomedical applications. Analyst, 147(11), 2294-2316.
[56] Trinh, T. N. D., Do, H. D. K., Nam, N. N., Dan, T. T., Trinh, K. T. L., & Lee, N. Y. (2023). Droplet-Based Microfluidics: Applications in Pharmaceuticals. Pharmaceuticals, 16(7), 937.
[57] Damiati, S., Kompella, U. B., Damiati, S. A., & Kodzius, R. (2018). Microfluidic devices for drug delivery systems and drug screening. Genes, 9(2), 103.
[58] Nisisako, T. (2016). Recent advances in microfluidic production of Janus droplets and particles. Current opinion in colloid & interface science, 25, 1-12.
[59] Mac Mahon, A. (2003). The Realms of Janus: Doorways in the Roman World. Theoretical Roman Archaeology Journal, (2002).
[60] Cheng, L., Cai, B., Zuo, Y., Xiao, L., Rao, L., He, Z., ... & Zhao, X. Z. (2017). Janus droplet parallel arrangements using a simple Y-channel flow-focusing microfluidic device. Chemical Physics Letters, 673, 93-98.
[61] Khan, I. U., Serra, C. A., Anton, N., Li, X., Akasov, R., Messaddeq, N., ... & Vandamme, T. F. (2014). Microfluidic conceived drug loaded Janus particles in side-by-side capillaries device. International Journal of Pharmaceutics, 473(1-2), 239-249.
[62] Kim, J. H., Jeon, T. Y., Choi, T. M., Shim, T. S., Kim, S. H., & Yang, S. M. (2014). Droplet microfluidics for producing functional microparticles. Langmuir, 30(6), 1473-1488.
[63] Korczyk, P. M., Dolega, M. E., Jakiela, S., Jankowski, P., Makulska, S., & Garstecki, P. (2015). Scaling up the throughput of synthesis and extraction in droplet microfluidic reactors. Journal of Flow Chemistry, 5(2), 110-118.

# 7 APPENDIX

## 7.1 SYRINGE PUMP

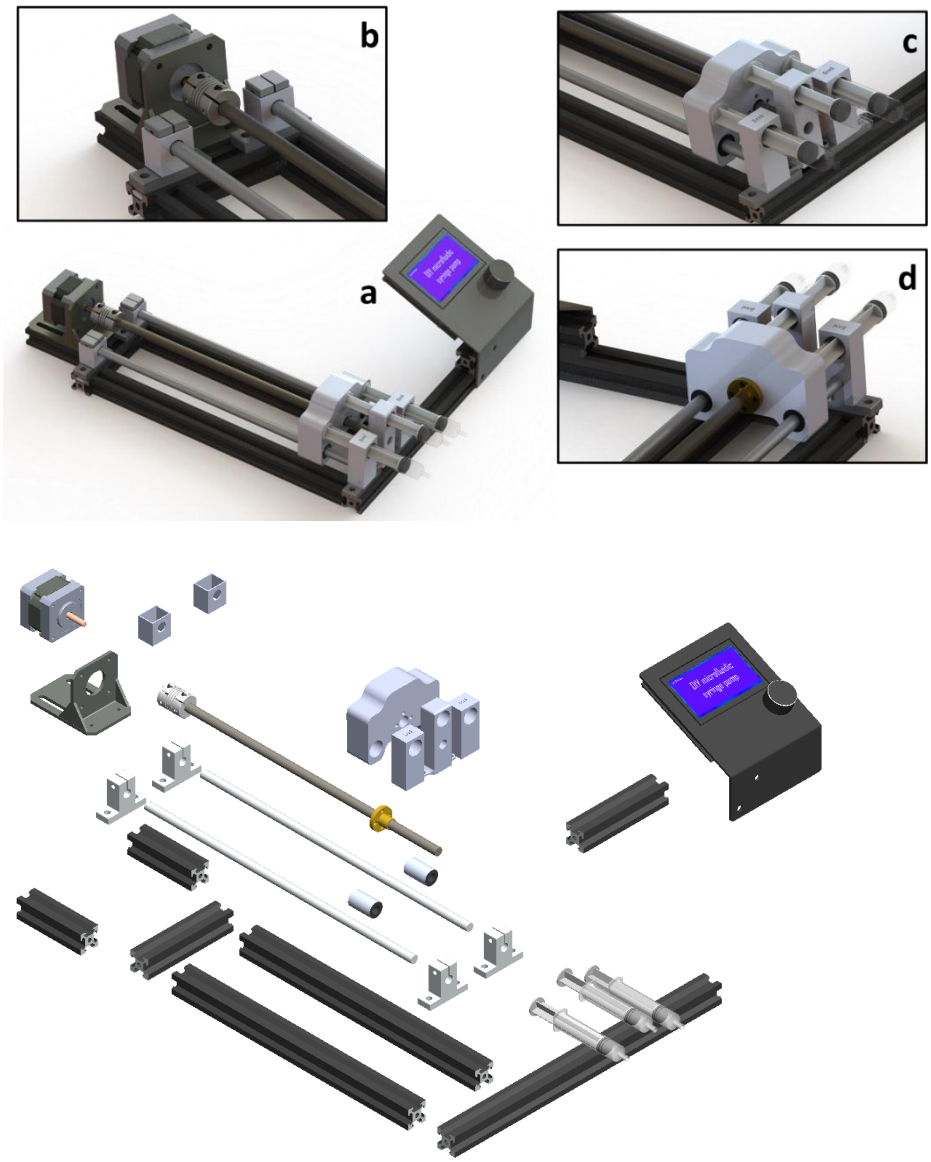


**Figure 27 (**Up) Photorealistic views of the syringe pump set up (down) Exploded view of the syringe pump. Parts with detailed description in Table 8

**Table 9** Syringe Pump Bill of Materials

| ITEM NO. | ITEM THUMBNAIL | PART NUMBER | QTY |
|---|---|---|---|
| 1 | 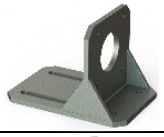 | STEPPER MOTOR MOUNT PLATE | 1 |
| 2 |  | STEPPER MOTOR | 1 |
| 3 | 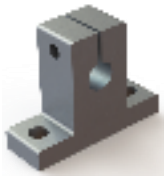 | LINEAR RAIL SHAFT GUIDE SUPPORT | 4 |
| 4 |  | PRECISION SHAFT - D8MM X L300MM | 2 |
| 5 |  | LINEAR BALL BEARING - 8MM DIAMETER - LM8UU | 2 |
| 6 |  | SHAFT COUPLER CLAMPING 5MM TO 5MM | 1 |
| 7 |  | TRIANGULAR M5X0.8 LEADSCREW | 1 |
| 8 |  | NUT FOR LEAD SCREW | 2 |
| 9 |  | PUSH BLOCK (3D PRINTED) | 1 |

| | | | |
|---|---|---|---|
| 10 | 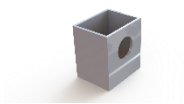 | COVER FOR LINEAR RAIL SHAFT GUIDE SUPPORT (3D PRINTED) | 2 |
| 11 |  | MID LEAD SCREW HOUSING FOR 5ML SYRINGE (3D PRINTED) | 1 |
| 12 | 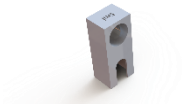 | SIDE ROD STOPS FOR 5ML SYRINGE HOUSING (3D PRINTED) | 2 |
| 13 |  | V-2020 ALLUMINUM PROFILE 72MM | 2 |
| 14 | 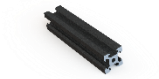 | V-2020 ALLUMINUM PROFILE 95.81MM | 2 |
| 15 |  | V-2020 ALLUMINUM PROFILE 260 MM | 2 |
| 16 |  | V-2020 ALLUMINUM PROFILE 300MM | 1 |
| 17 |  | TEE NUT 5MM | 8 |
| 18 |  | LCD | 1 |
| 19 |  | 5ML SYRINGE | 3 |

## 7.2 CHITUBOX SOFTWARE

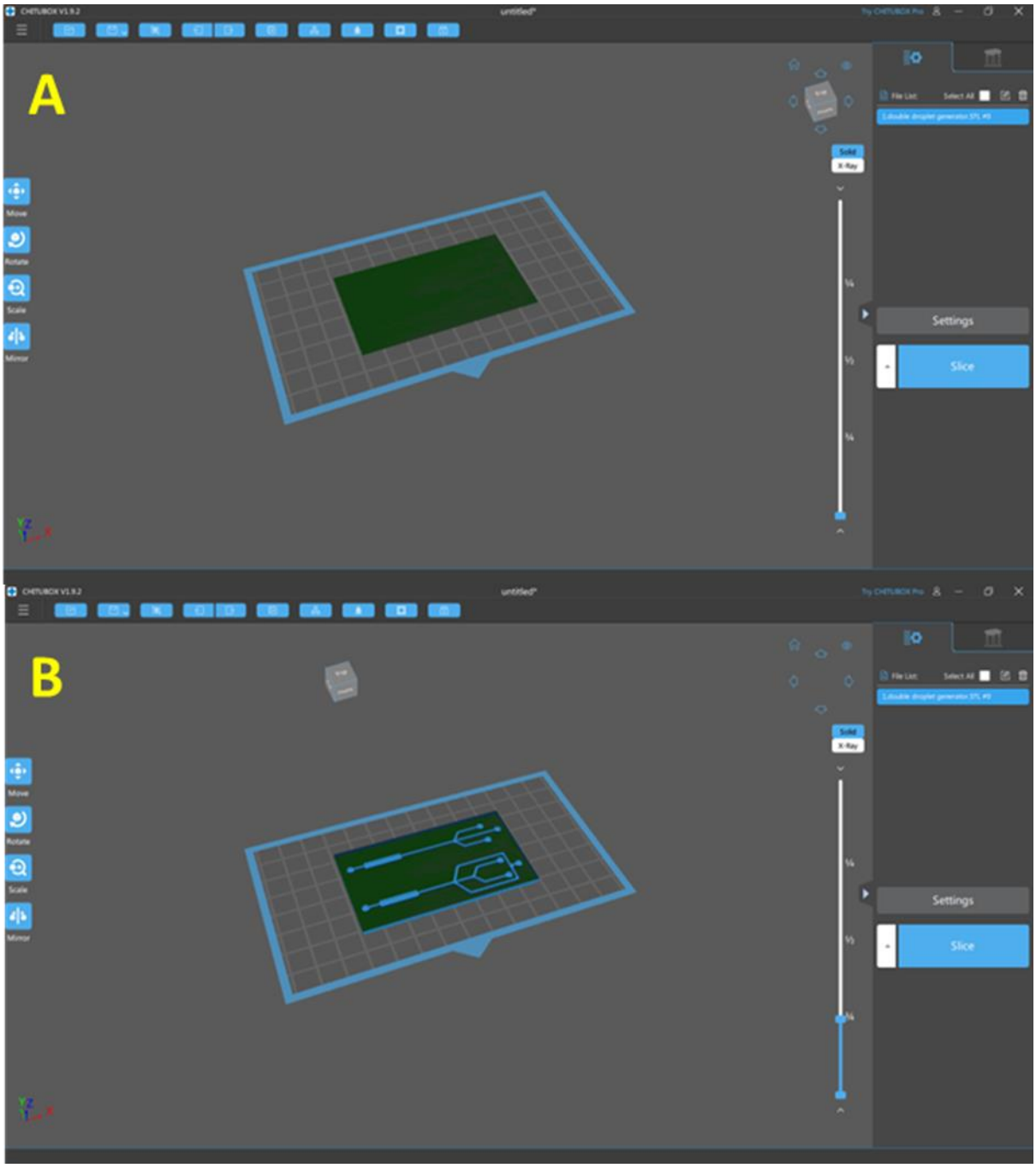


**Figure 28** Chitubox Slicer software interface. (A) First layer of the microfluidic device which is placed parallel to the build plate platform of the 3D printer. With green colour, the software in this stage, denotes the unmasked pixels of the LCD from which the light and solidifies the photosensitive resin. (B) Microchannels' first layer. With blue colour are denoted the masked layers form which no light penetrates.

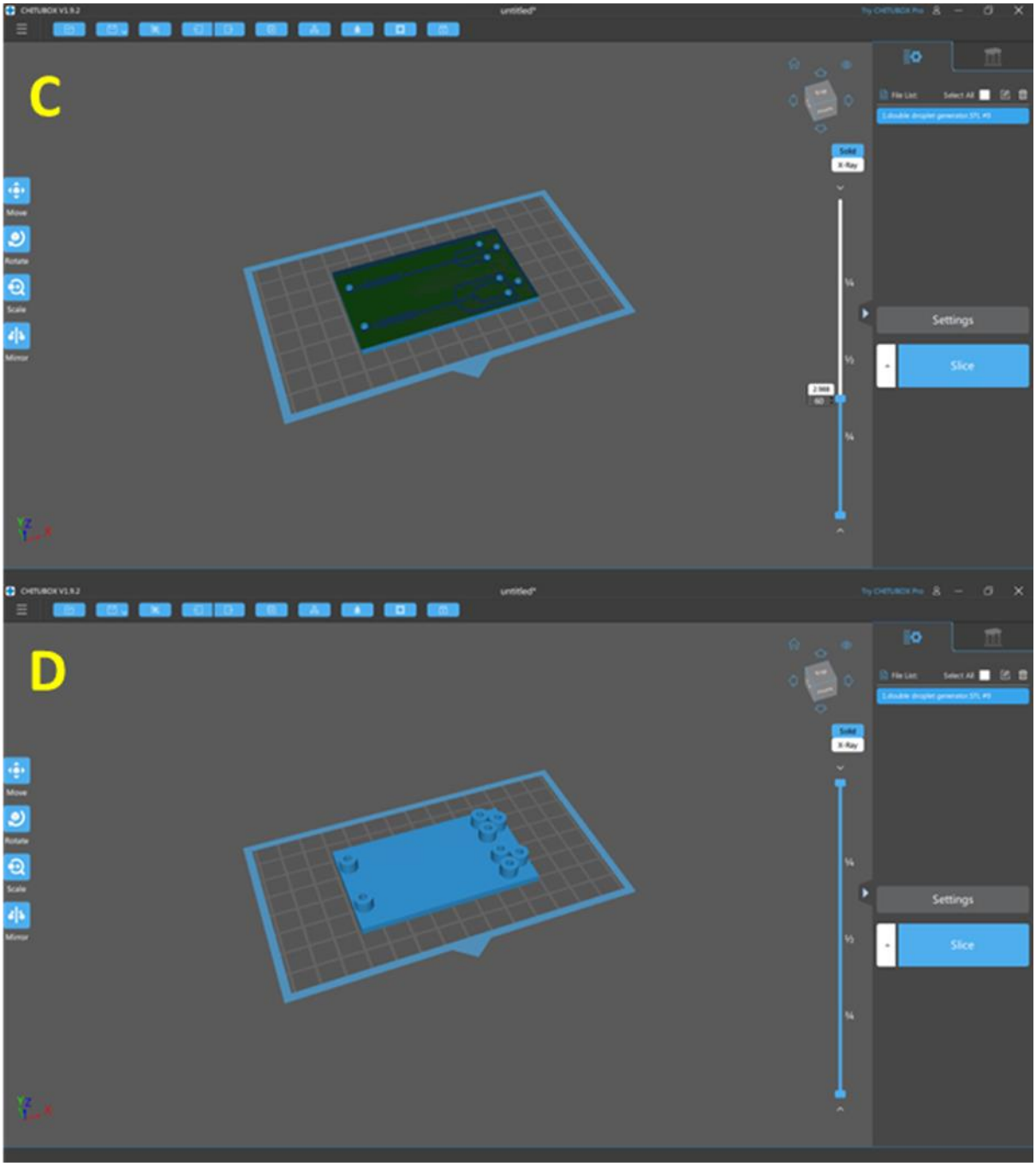


**Figure 29** (C) The first layer of the microchannels' sealing cup. (D) Preview of the final microfluidic device after 3D printing process.

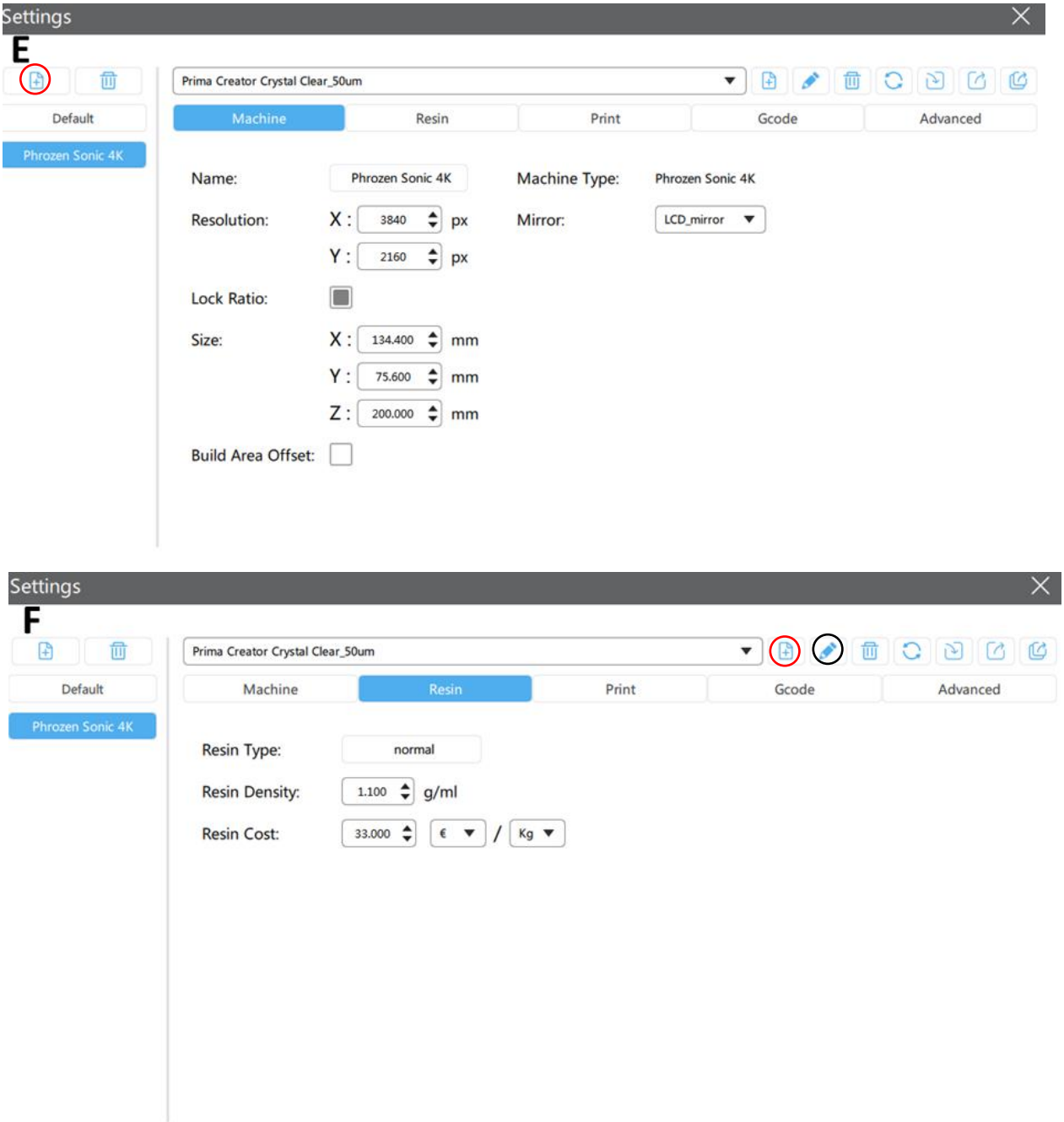


**Figure 30** When the STL file is loaded and placed properly onto the surface of the built plate. The printings settings have to be set (E) *Resin Tab*: In this tab, all the necessary information regarding the 3D printer are automatically updated after choosing the right machine from the first right icon (inside the right circle). If a 3D printer is not part of this data base or it is a custom-made LCD/DLP machine, then it can be manually created it by pressing the pencil symbol (inside the black circle). (F) After chosen the correct 3D printer, it is necessary to select correct resin. The icon inside the red circle allows the access in some predefined commercially available resins. If a resin is not part of this data base or it is a custom-made resin, then it can be manually created it by pressing the pencil symbol (inside the black circle).

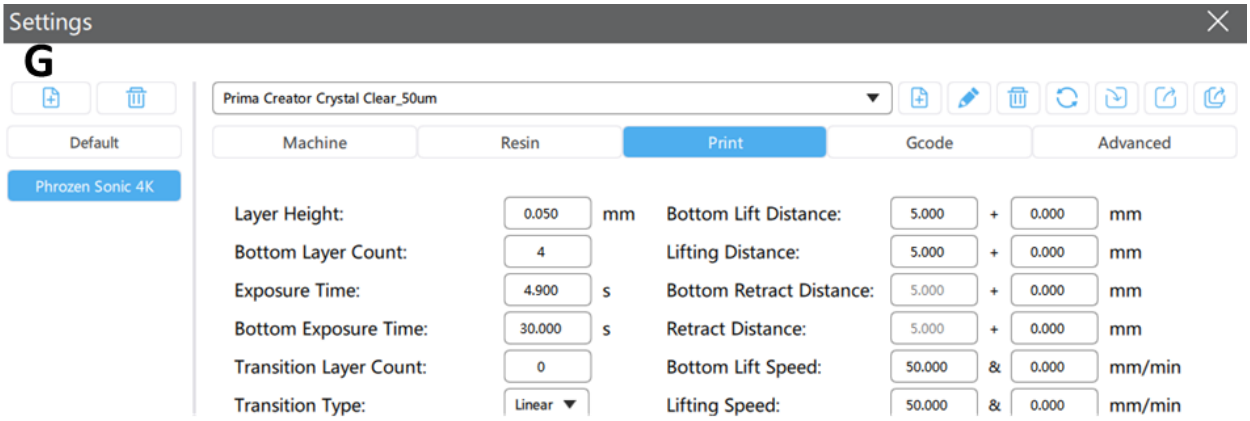


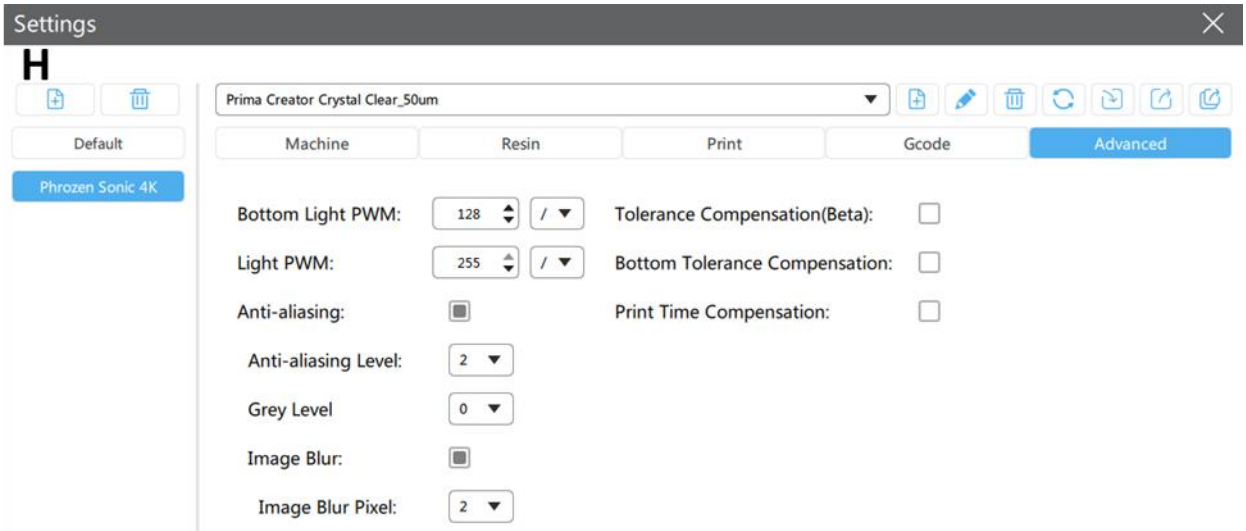


**Figure 31** (G) *Print Tab*: Here, the printing settings are selected based on the machine, resin and the STL file which is going to be printed (Detail explanation of each parameter, in the **Table 8.2**). (H) *Advanced Tab*: This tab is intended to offer a more advance options for the light source manipulation. More details about the above Tabs in https://manual.chitubox.com/en-US/docs/chitubox-basic/latest/setting-up/configure-print-parameters

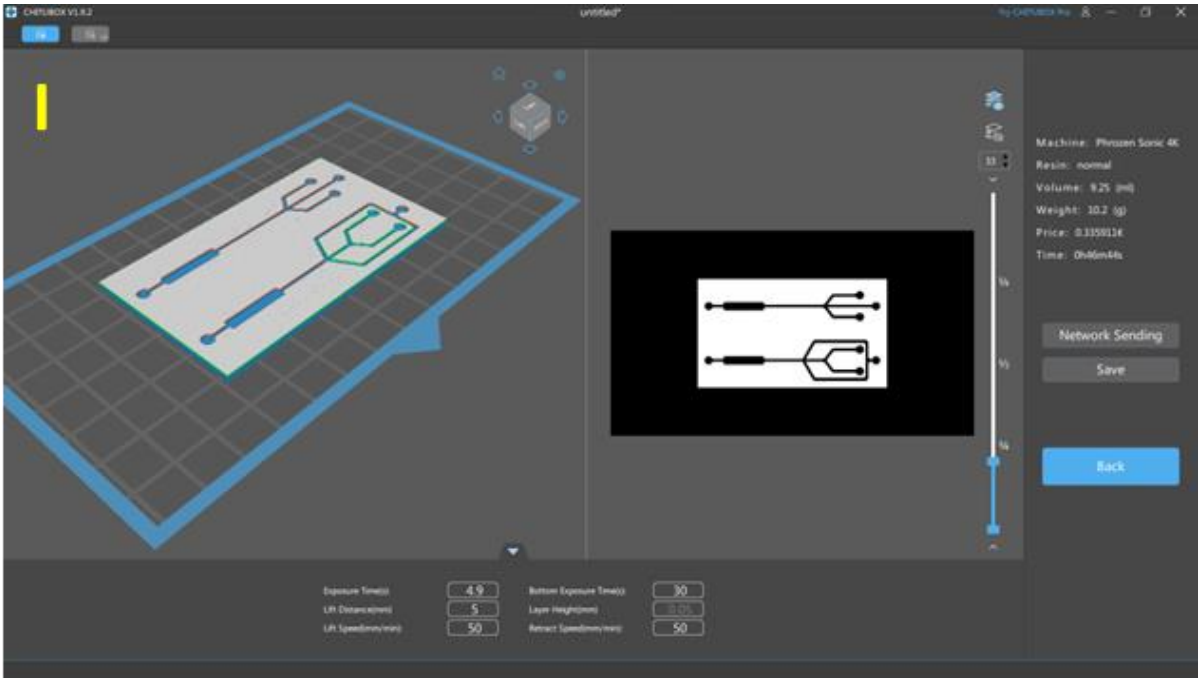


**Figure 32** The final Chitubox window in which is displayed a brief information about the name of the 3D printer and the resin used, the estimated resin volume required for the printing job, the total weight of the final part, a total price estimation based on the resin volume required and the time needed to finish the printing process. Also, in the bottom side six of the most important printing parameters are depicted as reminders of the selected process parameters. The black and white representation of the microfluidic device denotes the current layer. With black are all the masked pixels from which no light is passing through, while with white are every unmasked pixel on the LCD screen from which the UV light, from the paraled setup, penetrates and solidifies the photosensitive resin.

**Table 10** Detailed explanation of Chitubox printing process parameters (source: https://manual.chitubox.com/en-US/docs/chitubox-basic/latest/setting-up/configure-print-parameters#21-resting-time )

| PARAMETER | EXPLANATION |
|---|---|
| Layer Height | Thickness of each layer printed |
| Bottom Layer Count | The start printing layers. When the number of bottom layers is n, the exposure time of the first n layers is the exposure time of the bottom layers |
| Exposure Time | Exposure time of normal print layers |
| Bottom Exposure Time | Set the exposure time of the bottom layers. Increasing the exposure time of the bottom layers is helpful to increase the bond strength between the printing model and the printing platform |
| Transition Layer Count | The number of transition layers between the print bottom layers and the normal print layers. When printing in transition layers, the exposure time will decrease with the increase of printing layers |
| Transition Type | Set the transition type of the exposure time when transiting from the bottom layers to the normal layers |
| Waiting Mode During Printing | **Resting time**<br>• Rest Time Before Lift: A time interval between light-off and the build plate starts to lift.<br>• Rest Time After Lift: A time interval between the build plate has lifted to the Lifting Distance and starts to retract.<br>• Rest Time After Retract: A time interval between the build plete has retracted to the lowest point and light-on. |

| | |
|---|---|
| | **Light off delay**<br>Light-off delay is the total time of build plate lifts up, wait, and retract.<br><br>• Light-off Delay: Light-off delay for normal layers, True machine light-off time = maximum (total time of Z-axis up and down movement, configured light-off delay)<br>• Bottom Light-off Delay: Light-off delay for bottom layers, True machine light-off time = maximum (total time of Z-axis up and down movement, configured light-off delay) |
| | |
| Bottom Lift Distance | In the bottom layers printing process, the distance of the printing platform moves away from the printing surface each time |
| Lifting Distance | In the normal layers printing process, the distance of the printing platform moves away from the printing surface each time |
| Bottom Retract Distance | In the bottom layers printing process, the distance of retract, leave it alone unless you have sufficient reason |
| Retract Distance | In the normal layers printing process, the distance of retract, leave it alone unless you have sufficient reason |
| Bottom Lift Speed | In the bottom layers printing process, the speed of the printing platform moves away from the printing surface each time |
| Lifting Speed | In the normal layers printing process, the speed of the printing platform moves away from the printing surface each time |
| Bottom Retract Speed | In the bottom layers printing process, the speed of the printing platform moves to the printing surface each time |
| Retract Speed | In the normal layers printing process, the speed of the printing platform moves to the printing surface each time |